A PCA spatial pattern based downscaling approach for urban flood risk assessment

Julie Carreau, V. Guinot

To cite this version:

Julie Carreau, V. Guinot. A PCA spatial pattern based downscaling approach for urban flood risk assessment. 2020. hal-02903282v1

HAL Id: hal-02903282
https://hal.science/hal-02903282v1

Preprint submitted on 20 Jul 2020 (v1), last revised 8 Dec 2020 (v2)

A PCA spatial pattern based downscaling approach for urban flood risk assessment

J. Carreau

HSM, CNRS, IRD, Univ. Montpellier, France

V. Guinot

HSM, CNRS, IRD, Univ. Montpellier, France

Inria LEMON, Inria, Univ. Montpellier, France

Abstract

With CPU times reduced by two to three orders of magnitude compared to shallow water models, porosity models are considered as efficient tools for the modelling of urban floods on the scale of a conurbation. However, they provide only upscaled hydraulic fields that yield unreliable estimates of the flood risk in terms of financial losses and hazard to human lives. Downscaling of the porosity model simulation outputs is thus necessary. The present work puts forward a downscaling approach based on the decomposition of microscopic hydraulic fields into linear combinations of spatial patterns. The coefficients of the linear combinations are predicted with an Artificial Neural Network (ANN) whose input is derived from macroscopic hydraulic fields. Principal Component Analysis is used both to decompose the microscopic fields into linear combinations of spatial patterns and to project the macroscopic fields into lower dimensional features that are fed to the ANN. This global downscaling approach, which reconstruct the whole microscopic field at once, is compared with a local downscaling approach that relies on a similar setup except that each cell of the microscopic field is estimated separately by a dedicated ANN and that there are as many ANNs as cells. The two downscaling approaches are evaluated and compared at estimating the water depth and the norm of the unit discharge on five synthetic urban configurations and one field-test case. The analyses in terms of absolute errors show that the global approach not only provides a valid downscaling scheme but outperforms, in almost all instances, the local approach.

Keywords: Shallow water models, Porosity models, Flow variables for risk assessment, Downscaling at multiple locations, Artificial Neural Networks, Principal Component Analysis

---

1. Introduction

Two-dimensional shallow water models are widely accepted as a reference approach to the modelling of urban floods. However, they remain too computationally demanding in the current state of computer technology to be applicable to entire conurbations within reasonable computational times. For this reason, upscaled shallow water models have been under development over the past two decades. The earliest upscaled shallow water models were initially developed for the simulation of flows over microtopography and in channels [3, 4, 19]. Versions specifically dedicated to the modelling of urban floods, known as "porosity models", were later developed [9, 25, 26, 24, 27, 47, 38]. A salient advantage of shallow water models with porosity is their computational efficiency, with CPU times two to three orders of magnitude smaller than those of classical shallow water models [22, 25, 33]. Porosity models use computational cells that are typically 10 to 10^2 times as wide as those of classical two-dimensional models. As a consequence, the computational cell of a porosity model contains not only the water domain, but also buildings and other solid domains in which the flow is zero. The flow equations are solved on the average over the cells, the areas occupied by the solid phase being accounted for via statistical, geometric indicators such as porosities. The earliest versions of the model were developed using a single porosity [19, 24, 27]. More elaborate versions using storage and connectivity porosities [38, 47, 9, 25] or multiple porosities [22] were later proposed. Other upscaled versions such as the BCR/CRF model [16] use different indicators, the structure and function of which, however, bear similarities with the Integral Porosity model [38]. The price to pay for the computational efficiency of a porosity model is the coarseness of the approach. Porosity models provide simulation results in the form of upscaled (or averaged) flow variables over computational cells the size of a house to that of a building block.

For practical purposes, the knowledge of the flow fields is required with a much finer resolution. This is the case in particular with flood risk mapping. The flood risk results from the combination of local hydrodynamic factors (such as people's, buildings' and goods' vulnerability to the flood hazard) and hydrodynamic variables (derived from the water depths and flow velocities). As such, it cannot be inferred from the sole knowledge of averaged flow fields. A first example is that of the assessment of financial flood damage to buildings. The water depth is widely recognized as a prominent factor in flood damage modelling [8, 30, 36, 35, 43]. The damage to buildings is reported to be highly non-linear with respect to the water depth, which is reflected in most micro-scale flood damage models [44]. Consequently, using average depth values alone cannot be expected to yield reliable vulnerability assessments. Failing to incorporate such non-linearity on coarser scales is known to provide substantially erroneous damage estimates [40]. A second example is that of pedestrian vulnerability. Pedestrians' mobility (and with it the likelihood that pedestrians might safely evacuate high risk areas) is known to be subjected to threshold-based behaviours. When certain flow variables or their combinations (such as the water depth, unit discharge and specific force per unit width) exceed given thresholds (that are usually functions of size, age, physical condition, standing attitude, clothing etc.), pedestrians are likely to slip, tumble or start floating [1, 6, 15, 14, 18, 21, 29, 31, 32, 34, 41, 45]. In such cases, considered as "danger situations", pedestrian evacuation is compromised and lives are at threat. The risk function takes the form of a step with respect to the local flow variables, a function for which spatial averaging is meaningless. Therefore, in cases such as the two aforementioned examples, a form of downscaling of the upscaled model simulations is needed to perform relevant risk assessment.

In the context of climate change studies, statistical downscaling methods are developed to bridge the gap between the low resolution of General Circulation Models (GCMs) which is in the order of hundreds of km and the resolution needed for impact studies, from tens of km down to station locations [2]. Conventional downscaling approaches are univariate, i.e. they seek to estimate a climatic variable at a single site, either a station or a grid cell, given information deduced from a simulation generated by a GCM [2]. Artificial Neural Networks (ANNs) have long been applied in this context [28]. ANNs are non-parametric non-linear regression algorithms that are considered as “universal approximators”, i.e. they can approximate any continuous function when trained on informative enough data and provided that the number of hidden neurons is selected adequately [7]. A choice has to be made concerning the subset of GCM grid boxes to use as input in the downscaling method. A common approach consists in selecting all the grid boxes in a sufficiently large region and to reduce their dimension with Principal Component Analysis (PCA) [2, 28]. More recent downscaling approaches perform a multivariate estimation by accounting for dependence structures, e.g. to estimate a climatic variable jointly in several sites. In [42], “Schaake shuffle” is applied to restore the empirical dependence structure present in a calibration data set thereby assuming that the co-occurrences of the ranks of the variables always remain the same. This assumption might be too restrictive in the urban flood risk context as the range of spatial patterns displayed by the flow field might vary according to values taken by the initial and boundary conditions. In contrast, [11] relies on univariate techniques applied iteratively to random projections of the climatic variables. It is not clear that this approach can scale to very high dimensions. Indeed, refined shallow water models simulate flow variables on meshes that can contain tens of thousands of discrete cells.

In this work, a statistical downscaling approach is proposed that relies on PCA to scale with the very high dimensions of the refined shallow water models’ simulations and on ANNs to tackle the potential non-linearities in the relationships between low and high resolution simulations. PCA is applied on the high resolution flow fields to learn a representative basis of spatial patterns. The PCA decomposition means that each high resolution field can be seen as a linear combination of spatial patterns. The coefficients of the linear combination can be thought of as low dimensional features. An ANN with a feed-forward architecture and a direct linear connection is set up to learn these low dimensional features that represent the high resolution flow field. The input of the ANN is, as described above, a projection in a lower dimensional space of the low resolution field obtained with PCA. This global downcaling approach that estimates the whole high resolution field at once is compared with a more conventional univariate approach used as a reference. In the reference approach, the flow variable of interest is estimated at each cell of the high resolution mesh separately by setting up as many ANNs as there are cells. These two statistical downscaling approaches are evaluated and compared on a number of typical flooding configurations (a configuration being defined as the combination of building geometry, initial and boundary conditions). Refined flow simulations are carried out and exact upscaled solutions are obtained by averaging each reference solution over a coarse grid. The focus of the downscaling algorithms is on two risk variables : the water depth and the norm of the unit discharge.

The paper is organised as follows. Section 2 presents the reference model, reviews the variables of interest in flood risk assessment and poses the upscaling problem. In particular, upscaling, an underlying concept to porosity models but never identified as such in the publications, is defined formally for the purpose of the present work. Section 2 ends by introducing the downscaling framework used for urban flood risk assessment. Section 3 is devoted to the downscaling approaches developed in the present work. Section 4 describes the five synthetic configurations and the field-scale test for which simulations of the refined and upscaled solutions are carried out. Section 5 reports the evaluation and the comparison of the two downscaling methods. In Section 6, a discussion of the results together with conclusions and research perspectives are presented.

2. Urban flood risk assessment

2.1. The shallow water model

In what follows, the reference, microscopic model is the two-dimensional shallow water model, written in conservation form as

$$\partial_t \mathbf{u} + \nabla . \mathbf{F} = \mathbf{s} \tag{1a}$$

$$\mathbf{u} = \begin{bmatrix} h \\ q \\ r \end{bmatrix}, \ \mathbf{F} = \begin{bmatrix} q & r \\ \frac{q^2}{h} + \frac{g}{2}h^2 & \frac{qr}{h} \\ \frac{qr}{h} & \frac{q^2}{h} + \frac{g}{2}h^2 \end{bmatrix}, \ \mathbf{s} = \begin{bmatrix} 0 \\ gh\left(S_{0,x} - S_{f,x}\right) \\ gh\left(S_{0,y} - S_{f,y}\right) \end{bmatrix} \tag{1b}$$

$$\begin{bmatrix} S_{f,x} \\ S_{f,y} \end{bmatrix} = \frac{n^2}{h^{10/3}} \left|\mathbf{q}\right| \mathbf{q} \tag{1c}$$

where g is the gravitational acceleration, h is the water depth, n is Manning's friction coefficient, $\mathbf{q} = (q, r)^T$ is the flow velocity vector, $(S_{0,x}, S_{0,y})^T$ and $(S_{f,x}, S_{f,y})^T$ are respectively the bottom and friction slope vectors.

2.2. Variables for risk assessment

The water depth h (and more specifically its maximum with respect to time) influences directly the local damage caused to buildings and private property [8, 36, 44, 43]. In addition to the water depth, the norm of the unit discharge vector $|\mathbf{q}|$ and the specific force per unit width f are considered key indicators for pedestrian safety assessment [1, 6, 15, 18, 21, 31, 32, 34, 39, 41, 45]. The water depth is also related to the liability of a pedestrian to start floating [18]. The unit discharge is a criterion for pedestrian instability related to tumbling (moment instability), while the specific force per unit width is an indicator for friction instability (slipping) [31]. Moreover, the specific force per unit width is also reported to influence pedestrian evacuation speed [29], an important issue to assess and simulate evacuation patterns during floods [6]. The hydraulic head has occasionally been mentioned as a criterion for vehicle stability. However, it is much less used than the specific force per unit width.

It is acknowledged that the above criteria might not be sufficient to fully characterise pedestrian stability. For instance, [14, 15] report situations where the classical, steady state-based human instability criteria described in previous publications are strongly inaccurate because of the non-stationary character of the flow. As a consequence, situations that would be considered as “safe” by applying the average value of $|\mathbf{q}|$ and f turn out to be hazardous when experienced in a real-world event. Moreover, the acceptable threshold for pedestrian stability is not only a function of the flow variables but also of the pedestrian’s age, weight and size, physical condition, *etc* . . . [18].

The analysis reported hereafter focuses on the water depth and the norm of the unit discharge vector, that are the most widely acknowledged indicators for flood risk and the easiest variables to measure or compute. More precisely, let ψ be the variable of interest for risk assessment derived from $\mathbf{u} = [h, q, r]^T$. In what follows

$$\psi = \begin{cases} h & \text{or} \\ |\mathbf{q}| = \sqrt{q^2 + r^2}. \end{cases} \tag{2}$$

2.3. Upscaling framework

As discussed in the introductory section, refined shallow water models such as presented in sub-section 2.1 are too computationally demanding to be run on large areas. For this reason, porosity-based models have been developed in the past years, with CPU times reduced by two to three orders of magnitude compared to refined 2D models. Porosity models, however, are only one of the many possible options for upscaling the two-dimensional shallow water equations. In what follows, upscaling is understood as a filtering problem, as in [20].

Consider a fine-scale (also called microscopic) model obeying a set of governing equations

$$\mathbf{L}_m \left(\Theta_m, \mathbf{u}_m\right) = 0 \tag{3}$$

where $\mathbf{L}_m$ is a (vector) differential operator forming the governing equations, Θ_m and $\mathbf{u}_m$ are the fine scale parameter and variable vectors. Note that the two-dimensional shallow water model (1a)-(1c) is a particular case of the general form (3).

Upscaling consists in deriving a model with macroscopic parameters and variables obeying a set of macroscopic governing equations

$$\mathbf{L}_M \left(\Theta_M, \mathbf{u}_M\right) = 0 \tag{4}$$

where the subscript M denotes the upscaled, or macroscopic, operator, parameter set and solution. By assumption, the scale of the fluctuations in $(\Theta_M, \mathbf{u}_M)$ is larger than that of the fluctuations in $(\Theta_m, \mathbf{u}_m)$. In other words, the fields $(\Theta_M, \mathbf{u}_M)$ are significantly smoother than the fields $(\Theta_m, \mathbf{u}_m)$. Upscaling is understood as the process of deriving $\mathbf{L}_M$ (model upscaling), Θ_M (parameter upscaling) and/or $\mathbf{u}_M$ (solution upscaling) from the known microscopic model (3).

The purpose of a successful upscaling is that the macroscopic solution variable $\mathbf{u}_M$ be “as close as possible" to the microscopic solution $\mathbf{u}_m$. Since $\mathbf{u}_m$ and $\mathbf{u}_M$ are usually defined using different space-time resolutions, upscaling involves a filtering process. The filtered variable at a point $\mathbf{x} = (x, y)$ is defined as

$$< \mathbf{u}_m > (\mathbf{x}) = \int_{\Omega} \mathbf{u}_m \left(\mathbf{x}'\right) f \left(\mathbf{x}, \mathbf{x}'\right) \mathrm{d}\mathbf{x}' \tag{5}$$

where $f\left(\mathbf{x}, \mathbf{x}'\right)$ is the filtering kernel and Ω is the solution domain. In the case of a perfect upscaling, one has

$$\mathbf{u}_M \left(\mathbf{x}\right) =< \mathbf{u}_m > \left(\mathbf{x}\right) \quad \forall \mathbf{x} \in \Omega. \tag{6}$$

The most widely used filter in the field of upscaled urban flood models is the averaging operator over the computational cells of the macroscopic model:

$$f\left(\mathbf{x}, \mathbf{x}'\right) = \frac{1}{|\Omega_i|} \epsilon_i(\mathbf{x}, \mathbf{x}') \quad \Rightarrow \quad < \mathbf{u}_m > (\mathbf{x}) = \frac{1}{|\Omega_i|} \int_{\Omega_i} \mathbf{u}_m \, \mathrm{d}\Omega_i \quad \forall \mathbf{x} \in \Omega_i \tag{7a}$$

$$\epsilon_i(\mathbf{x}, \mathbf{x}') = \begin{cases} 1 & \text{if} \quad (\mathbf{x}, \mathbf{x}') \in \Omega_i \times \Omega_i \\ 0 & \quad\;\;\, \text{otherwise} \end{cases} \tag{7b}$$

where Ω_i is the subdomain occupied by the ith computational cell in the macroscopic model and $|\Omega_i|$ is its area. In this approach, the subdomains $\{\Omega_i\}_i$ form a partition of the overall computational domain Ω. The filtered microscopic solution $< \mathbf{u}_m >$ is compared directly to the finite volume solution $\mathbf{u}_M$ of the macroscopic model over the computational cells [9, 25, 26, 33, 47]. Such a comparison is particularly meaningful when $\mathbf{u}_m$ and $\mathbf{u}_M$ are both conserved variables.

Perfect upscaling can be thought of as a particular upscaled solution achieved by applying the domain averaging (7a) to the microscopic solution:

$$\mathbf{u}_{M,i} = \frac{1}{|\Omega_i|} \int_{\Omega_i} \mathbf{u}_m \, \mathrm{d}\Omega \tag{8}$$

$\mathbf{u}_{M,i} = \left(h_{M,i}, q_{M,i}, r_{M,i}\right)^T$ thus denotes the average of the conserved flow variable vector over the subdomain Ω_i. In what follows, the upscaled solution is considered as perfect as defined in (8).

2.4. Downscaling framework

To obtain an operational framework, downscaling methodologies have to be developed in order to estimate, with low computational cost, high resolution variables needed for urban flood risk assessment, such as the ones in (2), from upscaled ones. It is assumed that an upscaled 2D shallow water model has been run for a given domain geometry with given initial and boundary conditions over a partition $\{\Omega_i; 1 \leq i \leq D\}$ of Ω into D subdomains and for sample times $\{t_k\}_k$ of the simulation period $[0, T]$. The averaged risk variable, denoted $\Psi_{i,k}$, is thus available over each subdomain $\Omega_i \subset \Omega$ and each time $t_k \in [0, T]$. In addition, let $\{\omega_j\}_j$ be the cells of a high resolution mesh within Ω that could be used to run a microscopic model.

Then, downscaling consists in estimating $\{\psi_{j,k}; \forall k, j\}$, the high resolution risk variable, from $\{\Psi_{i,k}; \forall k, i\}$ based on statistical relationships.

To calibrate these statistical relationships to perform downscaling as described, pairs of upscaled and microscopic simulations for a given configuration and various initial and boundary conditions must be available. The microscopic solution $\mathbf{u}_m$ is computed by solving the two-dimensional shallow water equations (1a)-(1c) numerically over a fine mesh $\{\omega_j\}_j$. In this work, the upscaled solution is the perfect solution obtained from (8) by averaging the refined simulation over the subdomains Ω_i. Once calibrated, it is assumed that the downscaling relationships can be applied to upscaled simulations for the same configuration but for initial and boundary conditions that were not necessarily seen during calibration.

3. Statistical downscaling approaches

A global downscaling approach whose output at any time t_k is an estimate of the whole field $\{\psi_{j,k}; \forall j\}$ of the high resolution risk variable is introduced in subsection 3.2. A local approach that performs downscaling for each cell of the high resolution grid separately is presented first in subsection 3.1 as some of its building blocks are also used in the global approach.

3.1. Local downscaling approach

This approach seeks to learn a relationship between information drawn from the whole low resolution risk field (i.e. over all subdomains) and the value of the high resolution risk field at a given cell, see Fig. 1a. There are as many relationships as cells. More precisely, at a given time t_k, let $\boldsymbol{\Psi}_k \in \mathbb{R}^D$ be the concatenation into a vector of $\{\Psi_{i,k}; 1 \leq i \leq D\}$, the averaged risk field over all subdomains deduced from the upscaled simulation. The dimension of $\boldsymbol{\Psi}_k$ can be reduced by performing a Principal Component Analysis (PCA) yielding a decomposition of the form

$$\boldsymbol{\Psi}_k = A\boldsymbol{\Phi}_k \Leftrightarrow \boldsymbol{\Phi}_k = A^T\boldsymbol{\Psi}_k \tag{9}$$

where $A \in \mathbb{R}^D \times \mathbb{R}^d$ with $d < D$ and $\boldsymbol{\Phi}_k \in \mathbb{R}^d$ is the low dimensional representation of $\boldsymbol{\Psi}_k$. The relationship between the pairs $\{(\boldsymbol{\Phi}_k, \psi_{j,k})\}_k$ is learned with an Artificial Neural Network (ANN). There are as many ANNs as cells j where ψ_j needs to be estimated.

The ANNs are implemented as shown in Fig. 2a with a standard feed-forward architecture that includes one hidden layer plus a direct linear connection such that the case with no neuron in the hidden layer boils down to classical linear regression [7]. More precisely, in Fig. 2a, the input layer consists of $\boldsymbol{\Phi} = (\Phi_1, \ldots, \Phi_d)$, the vector of dimension d of low dimensional features extracted by PCA from the upscaled simulation where the dependence on time, i.e. the subscript k, is dropped for convenience ; in addition, there is a special neuron in the input layer permanently set to 1 to account for constants in the calculations ; the hidden layer has N_h neurons denoted $a_1, \ldots, a_{N_h}$; the output layer has a single neuron that yields $\hat{\psi}_j$, an estimate to the value of the high resolution risk field value at the cell j. The weight vector $\boldsymbol{w}$ of the ANN includes the weight matrix $\boldsymbol{w}^{\text{hid}}$ of dimensions $(d+1) \times N_h$ connecting the input

(a) *Local approach : for each cell j, a dedicated ANN learns to estimate ψ_j, the high resolution risk field value at the cell j.*

(b) *Global approach : a single ANN learns to estimate $\boldsymbol{\phi}$, the PCA projection in a low feature space of $\boldsymbol{\psi}$, the high resolution risk field concatenated into a vector.*

Figure 1: *Common building blocks of the two downscaling approaches : PCA is applied to reduce the dimensionality of $\mathbf{\Psi}$, the low resolution risk field concatenated into a vector for a given time step, yielding the lower dimensional vector $\mathbf{\Phi}$ used as input vector for the ANN.*

layer to the hidden layer ; a weight vector $\boldsymbol{w}^{\text{out}}$ of length N_h connecting the hidden layer to the output layer and the weight vector $\boldsymbol{w}^{\text{lin}}$ of length $1+d$ that links directly the input layer to the output layer. The calculations performed at the hidden and the output layers, see Fig. 2a, are given respectively by

$$a_n(\mathbf{\Phi};\boldsymbol{w}_n^{\text{hid}}) = \tanh\left(\sum_{i=1}^{d} w_{n,i}^{\text{hid}}\Phi_i + w_{n,0}^{\text{hid}}\right) \qquad n = 1,\dots,N_h \tag{10}$$

$$\hat{\psi}_j(\mathbf{\Phi};\boldsymbol{w}) = g\left(\underbrace{\sum_{n=1}^{N_h} w_n^{\text{out}} a_n(\mathbf{\Phi};\boldsymbol{w}^{\text{hid}})}_{\text{non-linear}} + \underbrace{\sum_{i=1}^{d} w_i^{\text{lin}}\Phi_i + w_0^{\text{lin}}}_{\text{linear}}\right) \qquad \text{for a given } j, \tag{11}$$

where $g(\cdot) = \log(1+\exp(\cdot))$ serves to enforce positivity.

For each cell j, an ANN is trained by optimizing its weigths $\boldsymbol{w}$ so as to minimise, over a so-called training set made of pairs of the form $\{(\mathbf{\Phi}_k, \psi_{j,k})\}_k$, the following sum of squared errors :

$$\mathcal{E}_{\text{loc}}(\boldsymbol{w};j) = \frac{1}{2}\sum_k (\hat{\psi}_j(\mathbf{\Phi}_k;\boldsymbol{w}) - \psi_{j,k})^2. \tag{12}$$

A gradient descent optimisation algorithm is used resorting to the back-propagation algorithm to efficiently compute the gradient [37]. The optimisation is performed 10 times with random initial parameter values and the optimised parameters yielding the lowest error computed on the training set are retained.

The hyper-parameters in the local approach are the number of hidden units N_h in the ANN and the dimension d of the feature space derived from PCA, see (9). Indeed, they control the overall number of weights in the ANN which is directly related to the complexity level of the function that can be learned by the ANN. Therefore, for each cell j, suitable values for N_h

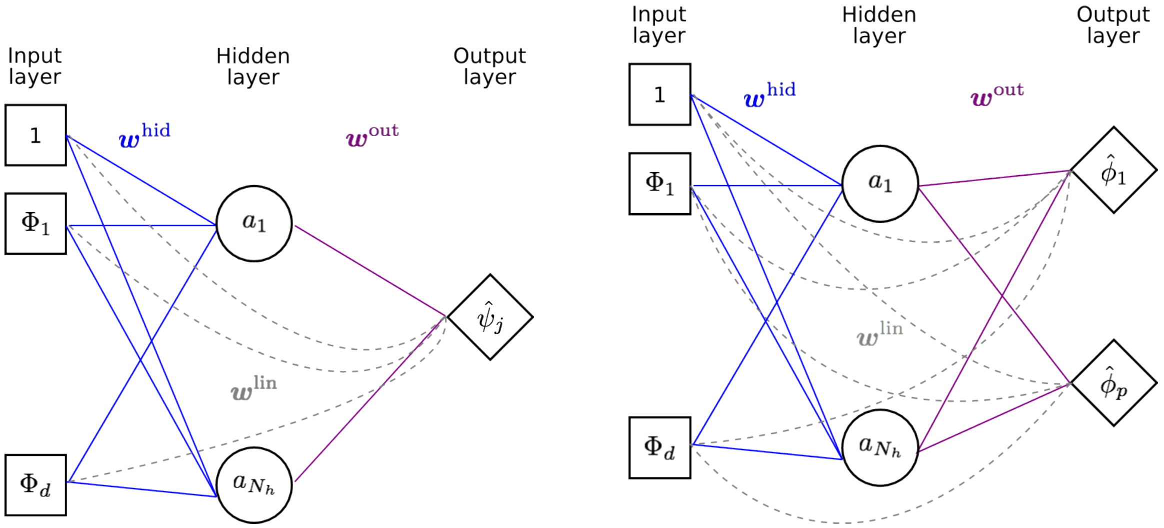

(a) *Local approach : one ANN for each cell j with a single output neuron that estimates directly the high resolution risk field value at the cell, see* (10)-(11).

(b) *Global approach : a single ANN whose output layer seeks to estimate a low dimensional representaton of the whole high resolution field, see* (10)-(14).

Figure 2: *Standard feed-forward artificial neural network architectures with one hidden layer plus a direct linear connection used in the two downscaling approaches.*

and d must be selected with a validation procedure that works as follows [7]. Several potential pairs of values are considered for the hyper-parameters. For each such pair of hyper-parameter values, the ANN's weights are optimized on the training set. The performance of the ANN associated to each particular choice of hyper-parameter values is evaluated in terms of the sum of squared errors as in (12) but computed on a validation set, a data set distinct from the training set. The hyper-parameter values yielding the lowest validation error are retained. As a result, different hyper-parameter values are likely to be selected for different cells when the complexity of the relationship learned by ANNs differ.

3.2. Global downscaling approach

This approach is based on the assumption that the high resolution risk field can be decomposed into a linear combination of spatial patterns. A single ANN seeks to estimate the weights of the linear combination based on the information drawn from the whole low resolution risk field, see Fig. 1b. As for the low resolution risk field, at a given time t_k, let $\boldsymbol{\psi}_k \in \mathbb{R}^P$, be the concatenation into a vector of $\{\psi_{j,k}; 1 \leq j \leq P\}$, the high resolution risk field, where P is the total number of cells of the high resolution grid. PCA is used again to obtain the following linear decomposition

$$\boldsymbol{\psi}_k = B\boldsymbol{\phi}_k \Leftrightarrow \boldsymbol{\phi}_k = B^T\boldsymbol{\psi}_k, \tag{13}$$

where $B \in \mathbb{R}^P \times \mathbb{R}^p$, $p < P$ and $\boldsymbol{\phi}_k \in \mathbb{R}^p$. The ANN in this approach seeks to learn the relationship between the pairs $\{(\boldsymbol{\Phi}_k, \boldsymbol{\phi}_k)\}_k$, see Fig. 2b.

To this end, the ANN's calculations at the hidden layer are as in (10) while at the output layer, the ANN has p neurons which perform the following calculations

$$\hat{\phi}_j(\boldsymbol{\Phi}; \boldsymbol{w}) = \underbrace{\sum_{n=1}^{N_h} w_{j,n}^{\text{out}} a_n(\boldsymbol{\Phi}; \boldsymbol{w}^{\text{hid}})}_{\text{non-linear}} + \underbrace{\sum_{i=1}^{d} w_{j,i}^{\text{lin}} \Phi_i + w_{j,0}^{\text{lin}}}_{\text{linear}} \quad j = 1, \ldots, p, \tag{14}$$

where, as previously, the time index k is dropped and $\boldsymbol{w}^{\text{out}}$ is a now a $N_h \times p$ matrix instead of a vector of length N_h. The size of the output layer and the absence of positivity constraints on the output neurons are thus the only differences with the architecture of the ANNs used in the local approach. For any time t_k, the estimated values of the high resolution risk field are given by

$$\hat{\boldsymbol{\psi}}(\boldsymbol{\Phi}_k; \boldsymbol{w}, B) = B\hat{\boldsymbol{\phi}}(\boldsymbol{\Phi}_k; \boldsymbol{w}), \tag{15}$$

where $\hat{\boldsymbol{\phi}}(\boldsymbol{\Phi}_k; \boldsymbol{w}) = (\hat{\phi}_1(\boldsymbol{\Phi}_k; \boldsymbol{w}), \ldots, \hat{\phi}_p(\boldsymbol{\Phi}_k; \boldsymbol{w}))$ are the ANN outputs as provided in (14) and $\boldsymbol{\Phi}_k = A^T \boldsymbol{\Psi}_k$, see (9).

Much like in the local approach except that there is a single ANN to train, the ANN's weigths $\boldsymbol{w}$ are optimized by minimising the following sum of squared errors :

$$\mathcal{E}_{\text{fea}}(\boldsymbol{w}) = \frac{1}{2} \sum_{j=1}^{p} \sum_{k} (\hat{\phi}_j(\boldsymbol{\Phi}_k; \boldsymbol{w}) - \phi_{j,k})^2. \tag{16}$$

The same optimisation strategy as in the local approach is used : best optimised parameters out of 10 runs of back-propagated gradient descent algorithm with random initialisations.

There are three hyper-parameters in this downscaling approach : N_h and d, as in the local approach, and p, the dimension of the feature space of the high resolution risk variable, see (13). These hyper-parameters must also be selected with a validation procedure, as described in the local approach's subsection. In this case, the sum of squared error that measures the performance on the validation set is different than the one in (16) used for training :

$$\mathcal{E}_{\text{tot}}(\boldsymbol{w}; B) = \frac{1}{2} \sum_{j=1}^{P} \sum_{k} (\hat{\psi}_j(\boldsymbol{\Phi}_k; \boldsymbol{w}, B) - \psi_{j,k})^2. \tag{17}$$

In contrast to (16), this validation error takes into account the impact of the choice of p, the dimension of the feature space of the high resolution risk variable.

4. Low and high resolution simulated data sets

4.1. Synthetic urban configurations

Five synthetic urban configurations are considered. They rely on a common layout consisting of a periodic array of length L made of building blocks (see Fig. 3 and Table 1). The buildings are aligned along the $x-$ and $y-$directions. The spatial period and building spacing in the $X-$direction ($X = x, y$) are denoted by L_X and W_X respectively. The computational domain Ω is discretised into a high resolution mesh with 62.5 cm $\times$ 62.5 cm square cells, for 46080 cells in total. The subdomains Ω_i used to derive the perfectly upscaled solution $\mathbf{u}_M$ (see

(8)) are delineated by connecting the centroids of the building blocks (dashed line in Fig. 3). There are 20 such subdomains in total. Other options are available for the definition of Ω_i. For instance, the subdomains might be centred around the building blocks, or shifted by any distance in the $x-$ and/or $y-$direction. Besides, Ω_i may include more than one $x-$ and/or $y-$ building period. The present choice is motivated by two main reasons: (i) the size $L_x \times L_y$ is the smallest possible one that keeps the averaging domain periodic, thus ensuring maximum spatial resolution for the upscaled solution, (ii) defining Ω_i by connecting the centroids of the buildings is consistent with the meshing strategies required by a number of porosity-based shallow water models, such as the IP or DIP models [25, 26, 38].

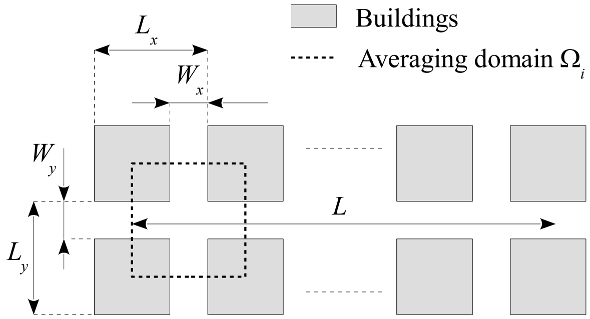

Figure 3: *Synthetic urban configurations : definition sketch for the geometry.*

Parameter	Meaning	Numerical value
L	Total domain length	1000 m
L_x	$x-$Period length	50 m
L_y	$y-$period length	50 m
W_x	Width of N-S streets	10 m
W_y	Width of E-W streets	10 m

Table 1: *Synthetic urban configurations : geometric parameters.*

In practice, the application of the downscaling approaches is restricted to the cells of the high resolution mesh that belong to three subdomains located slightly after the beginning, at the middle and slightly before the end of the computational domain. The subdomains' x-limits are [250 m, 300 m], [500 m, 550 m] and [750 m, 800 m]. Each subdomain contains 2304 cells for a total of 6912 cells considering the three subdomains. The global approach from subsection 3.2 is applied on the full set of 6912 cells. As the local approach described in subsection 3.1 requires to learn a separate relationship for each cell, the number of cells was reduced to 125 within each subdomain to keep the computation time within reasonable limits. For each of the three subdomains, the 125 cells are selected as follows, see Fig. 4. The subdomain is divided into 5 rectangular zones : one for the central crossroads and four for each of the branches departing from the intersection. Each of these five zones comprises 5×5 cells spread regularly so as to allow for a maximum coverage of the rectangular zone.

The first two synthetic configurations considered are 1D negative and positive waves without friction that are 1D Boundary Value Problems (BVPs). These configurations, identified as `N-wave-nf` and `P-wave-nf` respectively for short, are one of the simplest possible BVPs for layouts of this type. The frictionless propagation along the $x-$direction of a wave into still

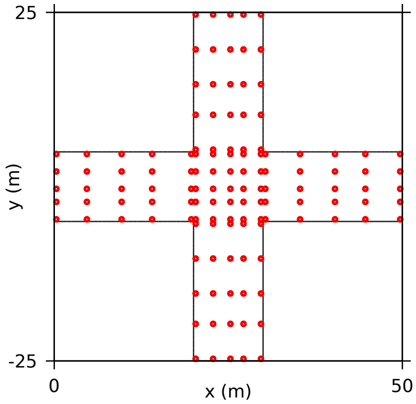

Figure 4: *Synthetic urban configurations : locations of the 125 cells within a given subdomain. The origin of the coordinates are taken from the SW corner of the subdomain.*

water is simulated (Fig. 5). The bottom is flat, the water is initially at rest in the domain, with an initial depth h_0. The water level is set instantaneously to a constant value h_1 at the Western boundary of the domain. In `N-wave-nf`, $h_1 < h_0$, which yields a negative wave (rarefaction wave). In `P-wave-nf`, $h_1 > h_0$ and a positive wave (shock wave) appears. The macroscopic solution $\mathbf{u}_M$ is self-similar in the (x, t) domain [23, 25, 26].

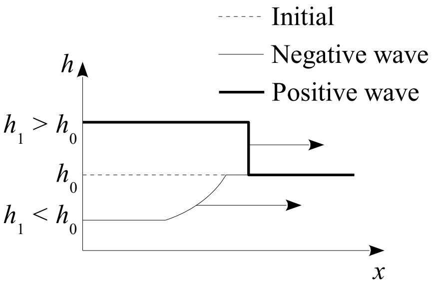

Figure 5: *Negative and positive wave configurations : initial and boundary condition definition sketch.*

The next two synthetic configurations use the same geometry as `N-wave-nf` and `P-wave-nf` (Fig. 5) but with a non-zero bottom friction coefficient. These configurations, identified as `N-wave-wf` and `P-wave-wf` respectively, are cases study closer to real-world situations. As a consequence of the non-zero friction coefficient, the upscaled solution is no longer self-similar in the (x, t) space. Both the microscopic and upscaled solutions and their spatial gradients span a different range of hydraulic configurations from that of `N-wave-nf` and `P-wave-nf`.

The last synthetic configuration, identified as `Dam-break`, is a 2D oblique urban dam break problem. The dam break problem is a Riemann, Initial Value Problem (IVP) where the water is initially at rest and the water depth is piecewise constant, equal to h_L and h_R respectively on the left- and right-hand sides of a broken, divide line with average orientation SE-NW (Fig. 6a). This results in an average flow field and wave propagation pattern oriented in the SW-NE direction. Since the flow is diagonal to the main street directions, fully meshing the domain involves as many block periods in both directions of space. This makes the mesh size and the subsequent computational effort prohibitive. The difficulty can be overcome [23] by meshing only a single block period in the transverse direction (Fig. 6b). The topology of the mesh is modified by connecting the Northern side of the ith lateral street (boundary segment N_i in the Figure) with the Southern side of the $i+1^{\mathrm{th}}$ lateral street (boundary segment S_{i+1} in Fig. 6b). While the upscaled solution of an urban dam break problem parallel to the main street axis is known to be self-similar in (x, t) [22, 25, 23], self-similarity disappears when the propagation is oblique with respect to the street axes [23].

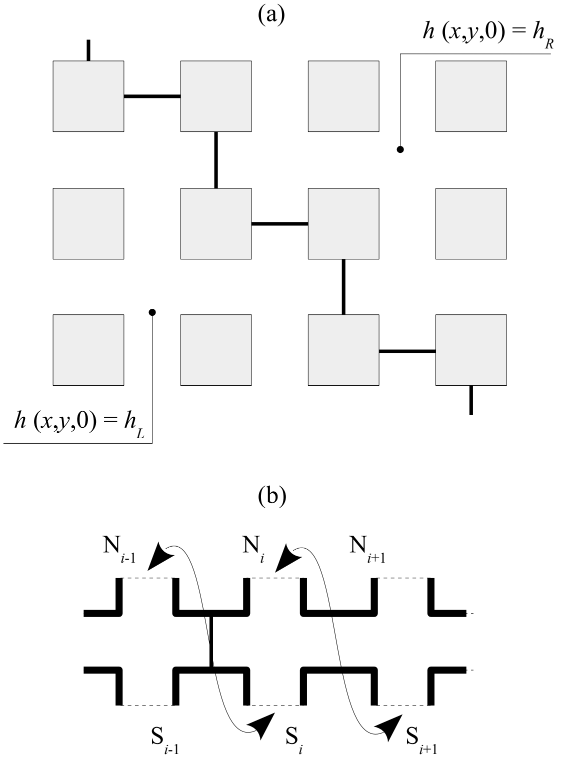

Figure 6: *2D oblique dam break problem. Definition sketch : (a) building layout and IVP geometry in plan view (b) periodic model mesh for computational efficiency. Bold lines: impervious boundaries. Dashed lines: boundary segments with staggered connection scheme.*

4.2. Field-scale test case

The field-scale test case considered was reported in [25] for the evaluation of a porosity-based, shallow water model. The propagation of a dike break flood wave into a neighbourhood of the Sacramento urban area is simulated. The test, which is referred to as `Sacramento` for short, is informative in many aspects: (i) the geometry is real, non-periodic, (ii) the upscaled hydraulic pattern is genuinely two-dimensional, and (iii) the microscopic flow field exhibits a strong polarisation along two preferential flow directions [25]. The dike breach is located on the left-hand side of the domain in Fig. 7. The Sacramento neighbourhood is discretised using a microscopic mesh made of 77 963 cells (average cell area 6.5 m^2). The macroscopic mesh used for upscaling is much coarser, with 1682 subdomains (average subdomain area 285 m^2). These two meshes are used for the refined and porosity-based shallow water simulations reported in Guinot *et al.* [25]. Fig. 8 shows close-up views of the microscopic and macroscopic meshes of the area where the 575 cells on which the local downscaling approach is applied are located. In contrast, the global downscaling approach is applied on the full set of 77 963 cells.

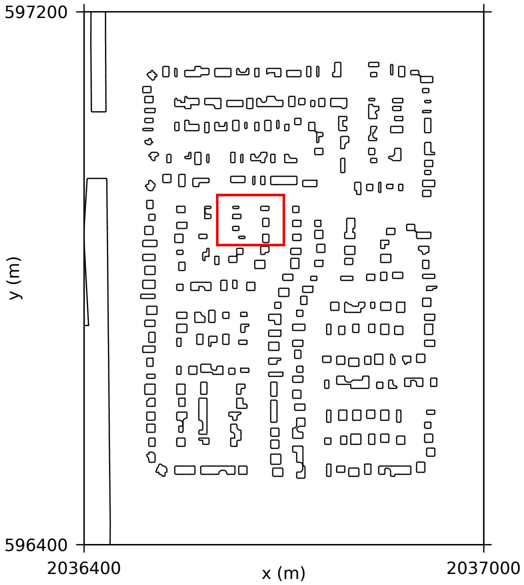

Figure 7: *Field-scale test : Sacramento neighbourhood with the bold rectangle indicating the zooming areas in Fig. 8.*

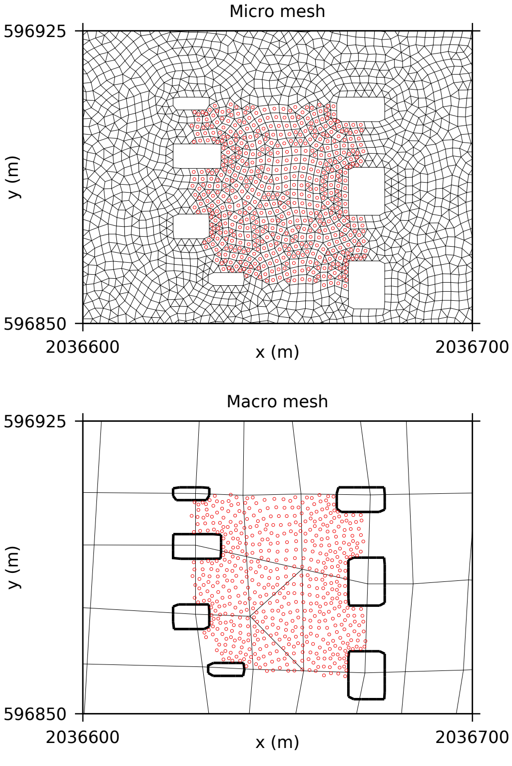

Figure 8: *Field-scale test (`Sacramento`) : area where the 575 cells (shown as red dots) on which the local downscaling approach is applied are located. Top: microscopic mesh. Bottom: macroscopic mesh.*

4.3. Training, validation and test sets

Training sets are defined to optimise the parameters of each downscaling approach (i.e. the ANNs' weights), validation sets to select optimal hyper-parameter values for each downscaling approach and test sets to compare the performance of the two downscaling approaches. These sets are made of a number of pairs of micro and macro simulations from the same configuration but with different values for the BC and/or IC. The underlying rationale is that, in a practical application, it is assumed that the configuration - such as positive or negative waves - can be known *a priori* but the appropriate values of BC and/or IC cannot. As a consequence, downscaling approaches should perform well, given a configuration, for any BC and/or IC values.

The values of BC and/or IC used to define the training, validation and test sets are labelled by a letter as indicated in Table 2 for the synthetic urban configurations and in Table 3 for the field-scale test. Fig. 9 illustrates the principle of the training-validation-test sets' design. The training set is designed so as to cover representative BC and/or IC values. For the synthetic urban configurations, there are three pairs of BC and/or IC values taken so as to form a right-angled triangle in the BC and/or IC space, see Fig. 9, whereas for the test-field case, there is a single initial condition for which two values are considered. The validation set includes two pairs of BC and/or IC values for the synthetic urban configuration taken as the midpoints of the two legs of the right-angled triangle while for the test-field case, a single value of the IC is considered for the validation set, the midpoint between the values forming the training set. The test set concerns BC and/or IC values that are different from those seen for training and validation. For the synthetic urban configurations, five such pairs of BC and/or IC values are considered. The field-scale test, in contrast, has only two possible IC values that form the test set.

Set	Label	`N-wave-nf / wf` (h_0, h_1) (m)	`P-wave-nf / wf` (h_0, h_1) (m)	`Dam-break` (h_L, h_R) (m)
Training	a	(1, 0.9)	(0.9, 1)	(3, 2.5)
	b	(1, 0.5)	(0.5, 1)	(3, 0.5)
	c	(0.6, 0.5)	(0.5, 0.6)	(1, 0.5)
Validation	d	(0.8, 0.5)	(0.7, 1)	(2, 0.5)
	e	(1, 0.7)	(0.5, 0.8)	(3, 1.5)
Test	f	(0.85, 0.75)	(0.65, 0.85)	(2.3, 1.2)
	g	(0.8, 0.4)	(0.7, 1.5)	(2, 0.01)
	h	(1, 0.7)	(0.3, 0.8)	(5, 1.5)
	i	(0.4, 0.3)	(0.3, 0.4)	(0.1, 0.01)
	j	(1.5, 1)	(1.3, 1.5)	(5, 4.5)

Table 2: *Training, validation and two test sets for the synthetic urban configurations in terms of BC and/or IC values. The BC and/or IC values for the negative waves* `N-wave-nf / wf` *are not exact mirrors of those for positive waves* `P-wave-nf / wf` *in order to ensure the feasibility of boundary condition prescription.*

Set	Label	h_0 (m)
Training	a	6 m
	b	4.5 m
Validation	c	5.25 m
Test	d	3.5 m
	e	7 m

Table 3: *Field-scale test (*`Sacramento`*). Values of h_0, the initial water depth in the channel, used to form the training, validation and test sets.*

The length of the simulation period T and the sampling time step are set as follows (see

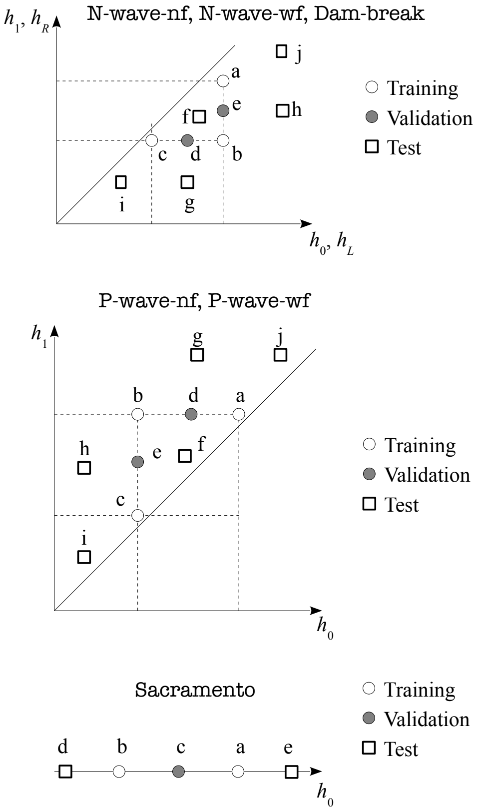

Figure 9: *Experiment plan definition sketch for each configuration.*

Table 2 for a compilation of the total number of time steps available for training, validation and test). The sampling time step is 10 s in configurations `N-wave-nf`, `N-wave-wf`, `P-wave-nf` and `P-wave-wf` and 5 s for `Dam-break` and `Sacramento`. For each synthetic urban configuration, the length of the simulation period may change with the BC and/or IC values so as to ensure that there is no wave reflection phenomena. The negative wave configurations, `N-wave-nf` and `N-wave-wf`, have a duration of 400 s - 41 time steps - for all BC and/or IC values except for the "j" one which is set to 260 s - 27 time steps. `P-wave-nf` has a duration of 300 s - 31 time steps -in call cases except for the BC and/or IC pair of values labelled "g" that has a time span of 200 s - 21 time steps. `P-wave-wf` has a duration of 300 s - 31 time steps - in all cases. `Dam-break` has a 100 s duration - 21 time steps - for all BC and/or IC values except the one labelled "j" that has a duration of 80 s - 17 time steps. The field scale simulation has a duration of 240 s - 49 time steps - except for the IC labelled "d" which spans 480 s - 97 time steps - to allow the water to reach most areas.

Configuration	Training	Validation	Test
`N-wave-nf`	123	82	191
`N-wave-wf`	123	82	191
`P-wave-nf`	93	62	145
`P-wave-wf`	93	62	155
`Dam-break`	63	42	101
`Sacramento`	98	49	146

Table 4: *Number of time steps available for training, validation and test for each configuration.*

5. Evaluation and comparison of downscaling methods

5.1. Principal spatial patterns

The global downscaling approach described in subsection 3.2 relies on the assumption that a representative enough basis of spatial patterns B in (13) can be identified with PCA. Before applying the global approach systematically, a preliminary analysis of the spatial patterns uncovered by PCA is presented in order to provide some insights into this approach. To this end, PCA is applied on the training set, see Table 2, and the first six Principal Components (PCs) are illustrated for each configuration. As PCs are adimensional, their value is relative to one another. The spatial patterns are computed for the two risk variables considered, i.e. the water depth and the norm of the unit discharge, see the discussion in subsection 2.2.

The dimension of the high resolution field, i.e. the number of cells in the fine mesh considered, is $P = 6912$ for the synthetic urban configurations and $P = 77\ 963$ for the field-scale test. For the synthetic urban configurations, only the subdomain located in the middle of the computational domain, with x-limits [500 m, 550 m], is shown, the other two subdomains have similar patterns. In addition, for the positive and negative waves, only the configurations without friction are shown, the ones with friction having similar albeit smoother patterns are deferred to Appendix A.

For `N-wave-nf`, the water depth has spatial patterns oriented along the x-direction on the horizontal branch, see Fig. 10. In contrast, the norm of the unit discharge exhibits complex spatial patterns along the y-direction on the vertical branches, see Fig. 11. For `P-wave-nf`, similar differences between the water depth and the norm of the unif discharge spatial patterns can be observed, see Figs. 12-13, though the patterns are more jagged. Similar remarks hold for `N-wave-wf` and `P-wave-wf`, see Figs. A.26-A.29. For `Dam-break`, the oblique orientation of the spatial patterns is visible for both the water depth and the norm of the unit discharge, see Fig. 14-15. Last, in Fig. 16-17, the spatial patterns of the water depth and the norm of the unit discharge for `Sacramento` are shown. Although the spatial patterns of the norm of the unit discharge are sharper than those of the water depth, the general shape, with the propagation of the water from the breach in the dike located at the top left (see Fig. 7), is similar for both risk variables.

5.2. Hyper-parameter selection

For the five synthetic urban configurations and the field-scale test, the hyper-parameters selected for the two downscaling approaches described in section 3 and for the two risk variables considered (water depth and norm of the unit discharge) are provided in Table 5. Several values are considered for each hyper-parameter so as to span the range of possibilities, starting from the lowest admissible value up to a value large enough to ensure that the selected value is not involuntarily bounded. The combination of all the values considered for each hyper-parameter are evaluated, i.e. the corresponding ANNs are trained, and the best combination, i.e. the one that yields the lowest validation error, is retained.

As expected, the number of spatial patterns (or equivalently, the number of PCs) selected is much lower when the risk variable is in a configuration yielding smoother dynamics, see the

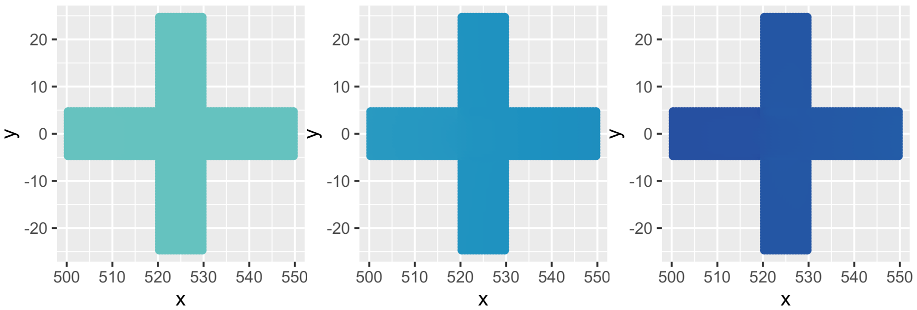

(a) *PC 1* **(b)** *PC 2* **(c)** *PC 3*

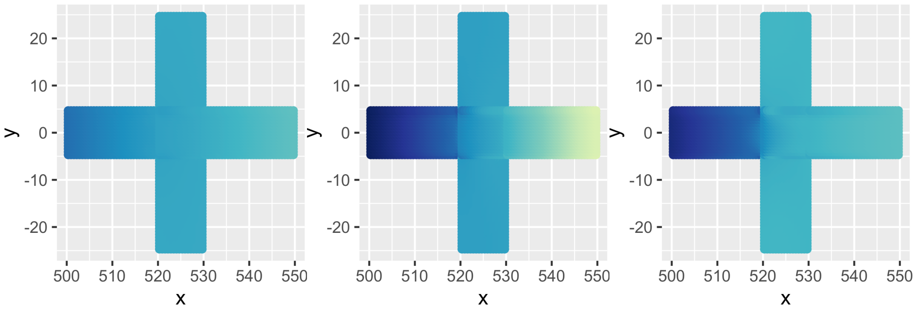

(d) *PC 4* **(e)** *PC 5* **(f)** *PC 6*

Figure 10: *Spatial patterns of the water depth for* `N-wave-nf` *obtained with PCA (first six PCs) over the subdomain located in the middle of the computational domain. The same adimensional color scale is used for all PCs.*

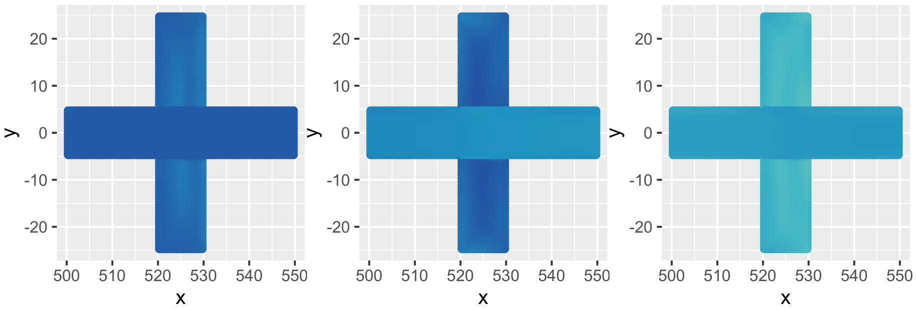

(a) *PC 1* **(b)** *PC 2* **(c)** *PC 3*

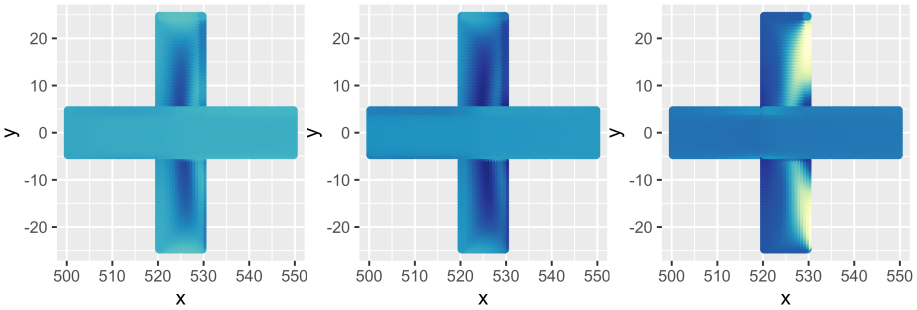

(d) *PC 4* **(e)** *PC 5* **(f)** *PC 6*

Figure 11: *Spatial patterns of the norm of the unit discharge for* `N-wave-nf` *obtained with PCA (first six PCs) over the subdomain located in the middle of the computational domain. The same adimensional color scale is used for all PCs.*

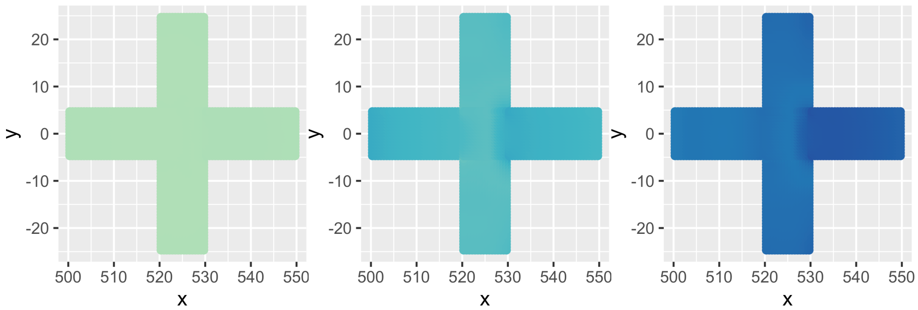

(a) *PC 1* **(b)** *PC 2* **(c)** *PC 3*

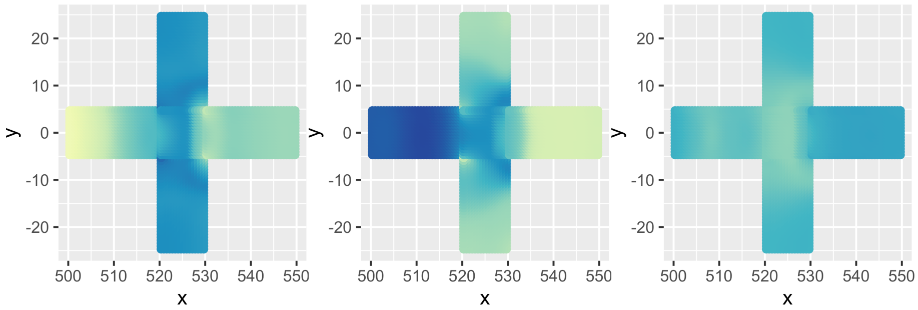

(d) *PC 4* **(e)** *PC 5* **(f)** *PC 6*

Figure 12: *Spatial patterns of the water depth for* `P-wave-nf` *obtained with PCA (first six PCs) over the subdomain located in the middle of the computational domain. The same adimensional color scale is used for all PCs.*

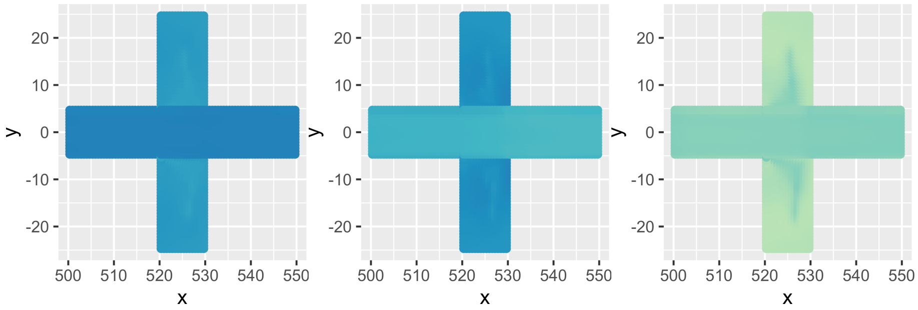

(a) *PC 1* **(b)** *PC 2* **(c)** *PC 3*

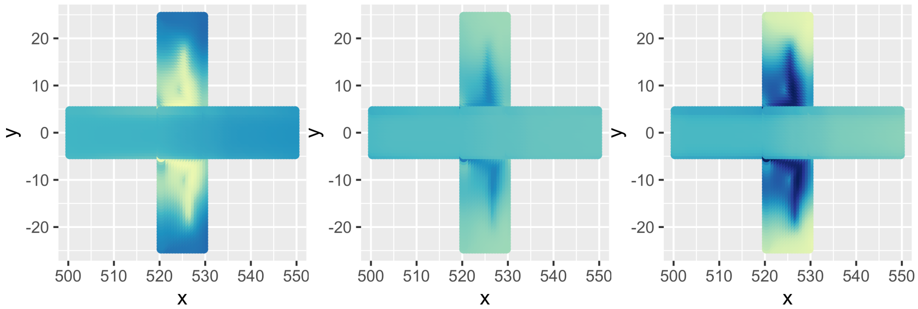

(d) *PC 4* **(e)** *PC 5* **(f)** *PC 6*

Figure 13: *Spatial pattern of the norm of the unit discharge for* `P-wave-nf` *obtained with PCA (first six PCs) over the subdomain located in the middle of the computational domain. The same adimensional color scale is used for all PCs.*

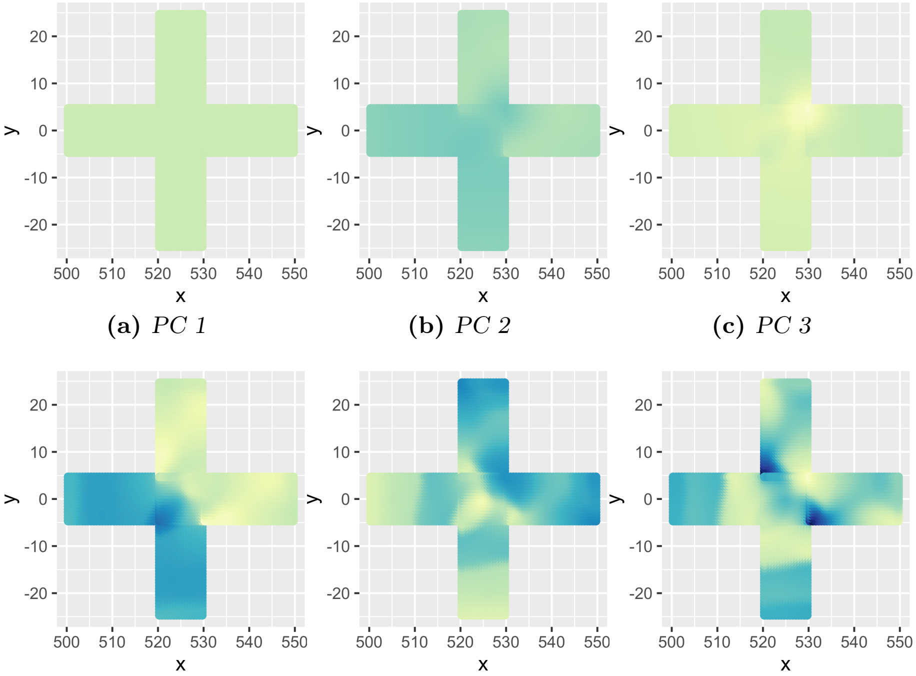

(a) *PC 1* **(b)** *PC 2* **(c)** *PC 3*

(d) *PC 4* **(e)** *PC 5* **(f)** *PC 6*

Figure 14: *Spatial patterns of the water depth for* `Dam-break` *obtained with PCA (first six PCs) over the subdomain located in the middle of the computational domain. The same adimensional color scale is used for all PCs.*

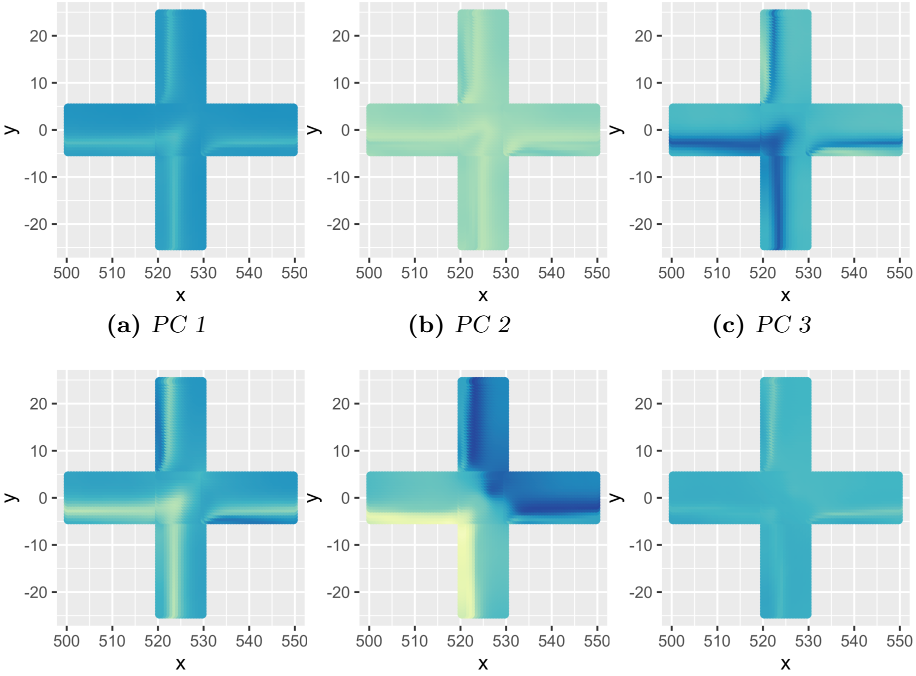

(a) *PC 1* **(b)** *PC 2* **(c)** *PC 3*

(d) *PC 4* **(e)** *PC 5* **(f)** *PC 6*

Figure 15: *Spatial patterns of the norm of the unit discharge for* `Dam-break` *obtained with PCA (first six PCs) over the subdomain located in the middle of the computational domain. The same adimensional color scale is used for all PCs.*

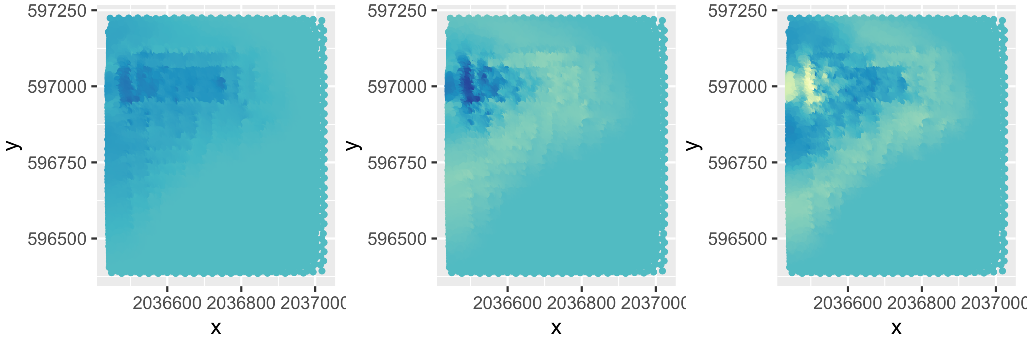

(a) *PC 1* **(b)** *PC 2* **(c)** *PC 3*

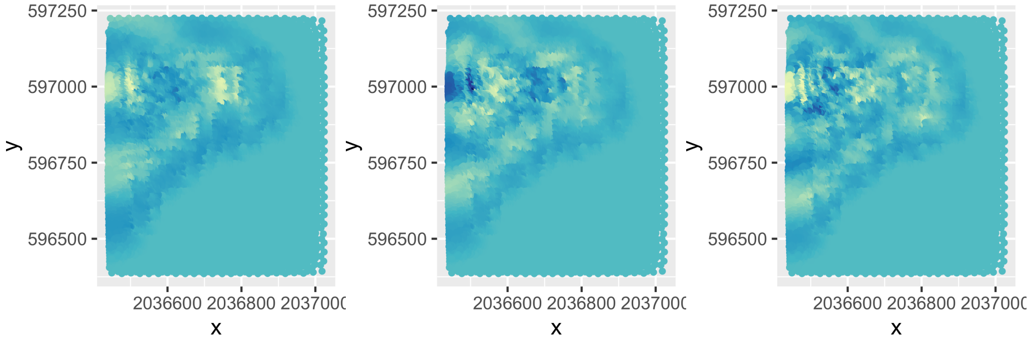

(d) *PC 4* **(e)** *PC 5* **(f)** *PC 6*

Figure 16: *Spatial patterns of the water depth for* `Sacramento` *obtained with PCA (first six PCs) over the subdomain located in the middle of the computational domain. The same adimensional color scale is used for all PCs.*

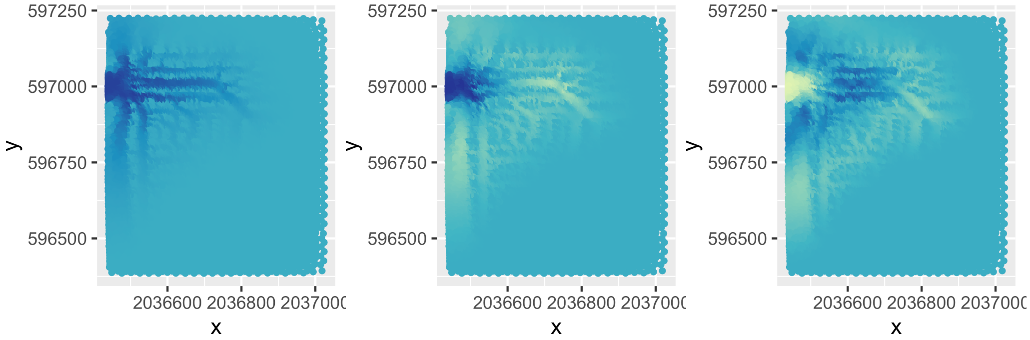

(a) *PC 1* **(b)** *PC 2* **(c)** *PC 3*

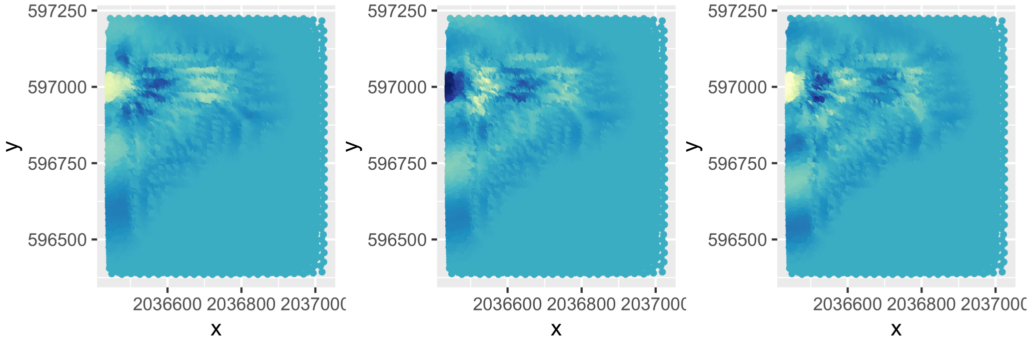

(d) *PC 4* **(e)** *PC 5* **(f)** *PC 6*

Figure 17: *Spatial patterns of the norm of the unit discharge for* `Sacramento` *obtained with PCA (first six PCs) over the subdomain located in the middle of the computational domain. The same adimensional color scale is used for all PCs.*

p-column of Table 5. This is the case for the water depth in the negative or positive wave configurations, with or without friction. In contrast, the water depth in the `Dam-break` and `Sacramento` configurations and the norm of the unit discharge, especially in the `P-wave-nf / wf` and `Sacramento` configurations, require higher numbers of spatial patterns. The only configuration in which the norm of the unit discharge requires less spatial patterns than the water depth is the `Dam-break` configuration. The input size and the number of hidden units of the ANNs, see the columns d and N_h in Table 5, in the local and global approaches are similar for `P-wave-nf / wf` but otherwise can be very different, see for instance the water depth in `N-wave-nf / wf`. The number of hidden units of the ANN in the global approach is almost always zero, indicating that a linear relationship is sufficient.

	Water depth					Norm of unit discharge				
Configuration	Local approach		Global approach			Local approach		Global approach		
	d	N_h	d	N_h	p	d	N_h	d	N_h	p
`N-wave-nf`	20 (0)	12 (16)	8	0	5	10 (5)	12 (19)	12	0	20
`N-wave-wf`	20 (0)	12 (16)	8	0	5	10 (5)	12 (18)	10	0	10
`P-wave-nf`	19 (1)	1 (4)	19	0	5	19 (3)	4 (14)	19	0	40
`P-wave-wf`	16 (3)	1 (1)	16	0	5	12 (3)	2 (4)	15	2	60
`Dam-break`	8 (10)	0 (1)	18	0	40	19 (6)	1 (8)	8	0	10
`Sacramento`	3 (3)	2 (0)	57	0	70	3 (12)	1 (1)	78	0	80

Table 5: *Selected hyper-parameters for each configuration : d input dimension, N_h number of hidden neurons and p output dimension, see Fig. 2. For the local approach, the median selected value is given with the inter-quartile range in parentheses.*

5.3. Test set comparisons

The comparison of the global and local approaches at downscaling the water depth and the norm of the unit discharge is carried on the test sets of each configuration, see Table 2, with the hyper-parameters selected on the validation sets, see Table 5. To this end, the ANNs of the local approach - one per cell - and the ANN of the global approach with the selected hyper-parameters are trained anew on a larger data set that merges together the training and validation sets. As in the subsection 5.1 on the spatial patterns uncovered by PCA, for the positive and negative waves, only configurations without frictions are shown, the ones with friction bring similar conclusions and are deferred to Appendix B.

For the water depth, the global approach performs generally better, as can be seen from the box-plots of the absolute errors for each test set provided in Fig. 18-21. One exception is `N-wave-nf`, see Fig. 18 (similarly for `N-wave-wf`, see Fig. B.30), for which the local approach performs slightly better for Test f, Test g and Test h but the overall absolute error is small ($< 8 \times 10^{-3}$ m). For Test i and Test j, the global approach performs better and the absolute error of the local approach jumps up to ≈ 0.5 m for Test j. For `P-wave-nf` shown in Fig. 19 (similarly for `P-wave-wf`, see Fig. B.31), the local approach performs worst on all test sets, especially Test g, Test h, Test i and Test j, with an absolute error up to ≈ 4 m, whereas the global approach's absolute error is bounded below 0.5 m for Test g and is much lower on the other test sets. For `Dam-break`, the global approach outperforms the local approach on most test sets although some test sets, such as Test g and Test h, are more challenging for both approaches, see Fig. 20. For `Sacramento`, the global approach also outperforms the local approach, especially for Test e, see Fig. 21.

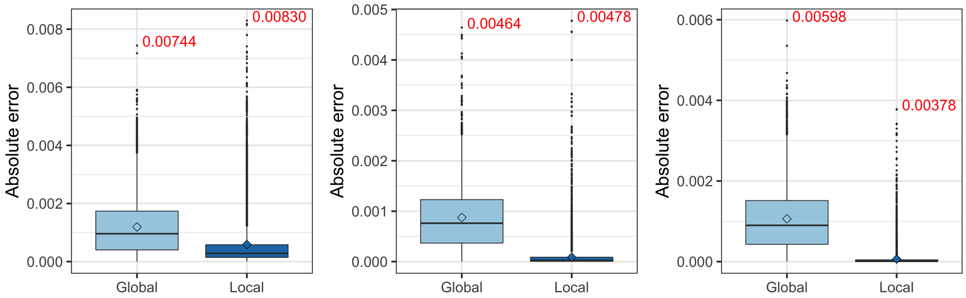

(a) *Test f* **(b)** *Test g* **(c)** *Test h*

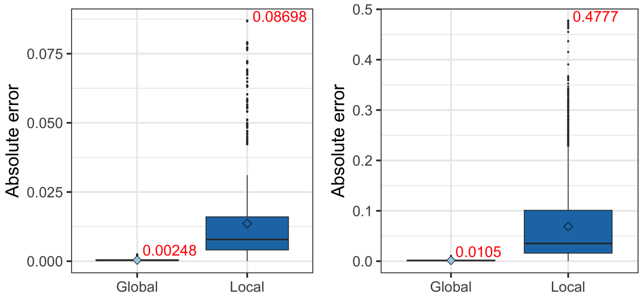

(d) *Test i* **(e)** *Test j*

Figure 18: *Downscaling of the water depth for* `N-wave-nf` *: box-plots of absolute errors for the global and the local downscaling approaches over the three selected subdomains (375 cells) for each of the five test sets, see Table 4. The maximum error is indicated in red over each box-plot.*

For the norm of the unit discharge, the global approach performs much better for all configurations and all test sets, see Fig. 22-25. For `N-wave-nf` in Fig. 22 (similarly for `N-wave-wf` in Fig. B.32), the absolute error for the global approach is bounded below 0.05 m^2/s. In contrast, the local approach's error exceeds 12 m^2/s for Test j. For `P-wave-nf` in Fig. 23 (similarly for `P-wave-wf` in Fig. B.33), one can observe that, again, the global approach has low absolute errors < 0.7 m^2/s whereas the local approach's absolute errors are very large, especially for Test f, Test g, Test h and Test j. Much like for the water depth, `Dam-break` is more challenging for both approaches, see Fig. 24. In particular, the global approach has an absolute error of up to ≈ 6 m^2/s on Test h but on the other test sets, the error is below $\approx$ 2 m^2/s or less. In contrast, the absolute errors of the local approach are very large, greater than 10 m^2/s for Test h and Test j. For `Sacramento`, much like for the water depth, the global approach outperforms the local approach with greated discrepancy between them for Test e, see Fig. 25.

6. Discussion and conclusion

We proposed a statistical model that is capable of downscaling very high dimensional fields such as the ones simulated by refined shallow water models, see subsection 3.2 and Fig. 1b

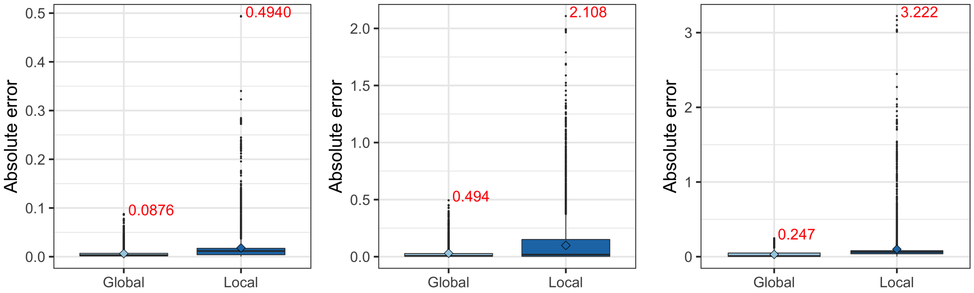

(a) *Test f* **(b)** *Test g* **(c)** *Test h*

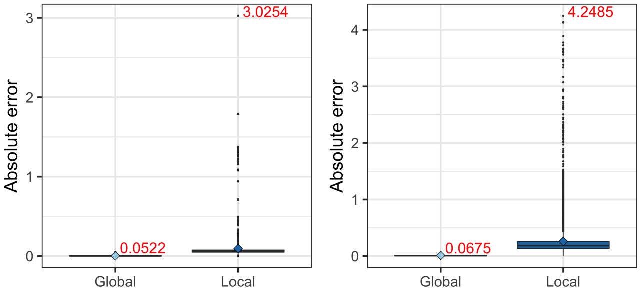

(d) *Test i* **(e)** *Test j*

Figure 19: *Downscaling of the water depth for* `P-wave-nf` *: box-plots of absolute errors for the global and the local downscaling approaches over the three selected subdomains (375 cells) for each of the five test sets, see Table 4. The maximum error is indicated in red over each box-plot.*

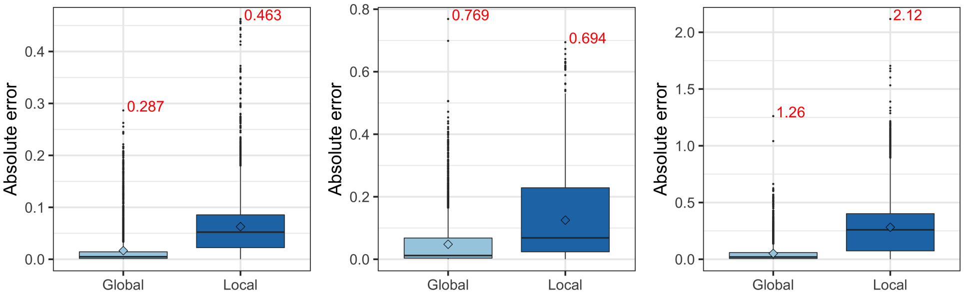

(a) *Test f* **(b)** *Test g* **(c)** *Test h*

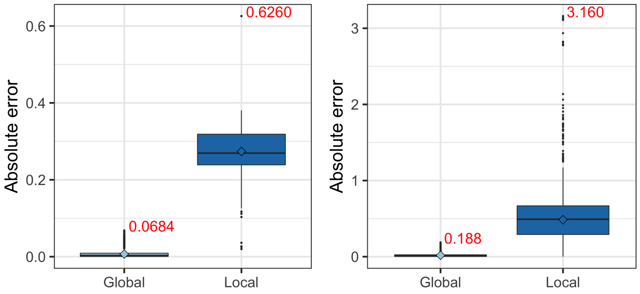

(d) *Test i* **(e)** *Test j*

Figure 20: *Downscaling of the water depth for* `Dam-break` *: box-plots of absolute errors for the global and the local downscaling approaches over the three selected subdomains (375 cells) for each of the five test sets, see Table 4. The maximum error is indicated in red over each box-plot.*

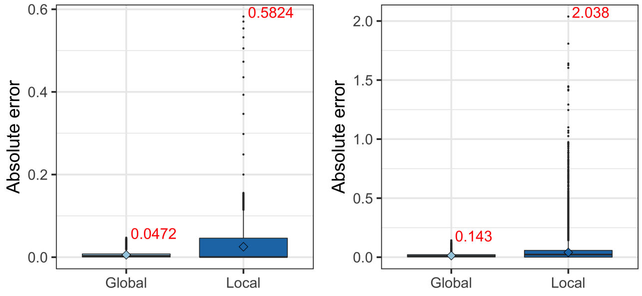

(a) *Test d* **(b)** *Test e*

Figure 21: *Downscaling of the water depth for* `Sacramento` *: box-plots of absolute errors for the global and the local downscaling approaches over the selected subregion (575 cells) for each of the five test sets, see Table 4. The maximum error is indicated in red over each box-plot.*

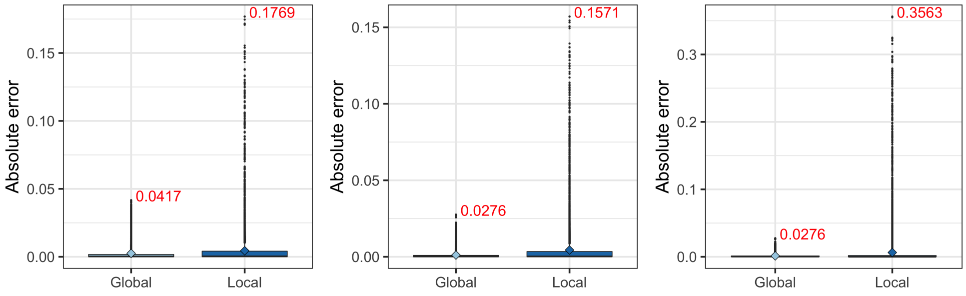

(a) *Test f* **(b)** *Test g* **(c)** *Test h*

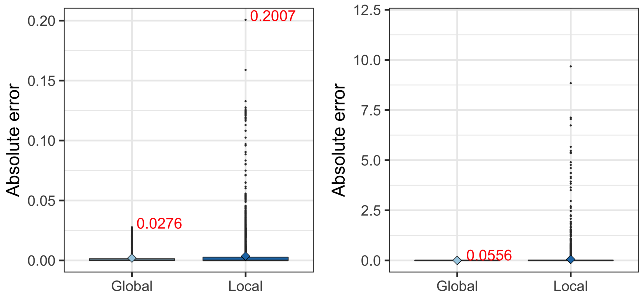

(d) *Test i* **(e)** *Test j*

Figure 22: *Downscaling of the norm of the unit discharge for* `N-wave-nf` *: box-plots of absolute errors for the global and the local downscaling approaches over the three selected subdomains (375 cells) for each of the five test sets, see Table 4. The maximum error is indicated in red over each box-plot. The scale is capped at 12.*

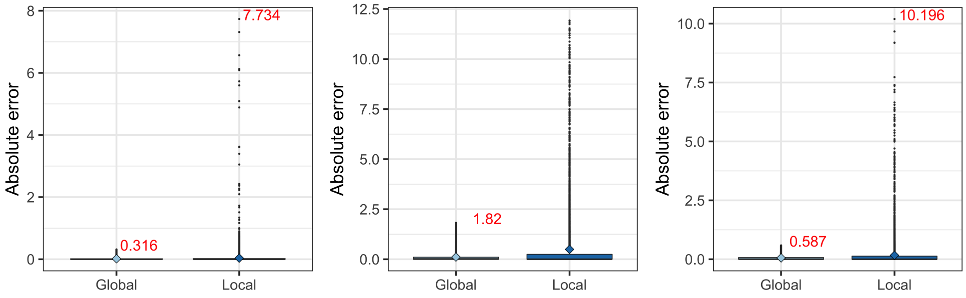

(a) *Test f* **(b)** *Test g* **(c)** *Test h*

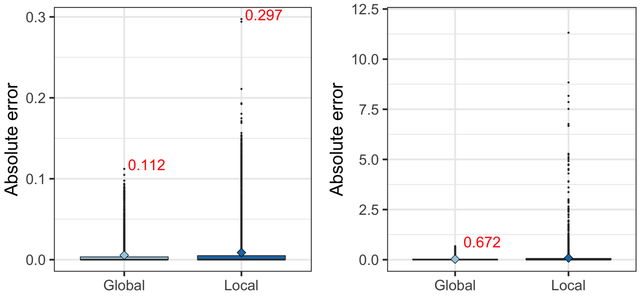

(d) *Test i* **(e)** *Test j*

Figure 23: *Downscaling of the norm of the unit discharge for* `P-wave-nf` *: box-plots of absolute errors for the global and the local downscaling approaches over the three selected subdomains (375 cells) for each of the five test sets, see Table 4. The maximum error is indicated in red over each box-plot. The scale is capped at 12.*

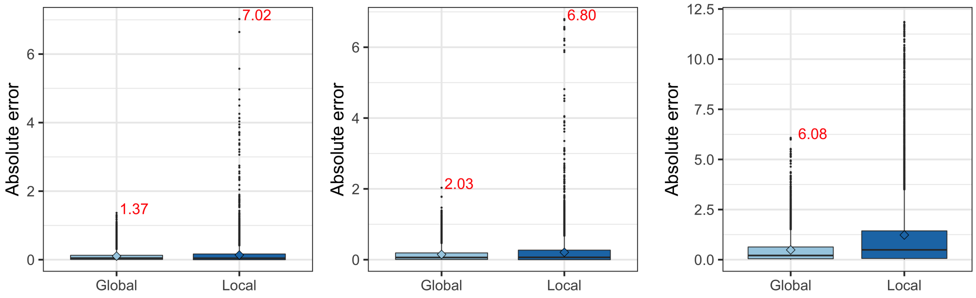

(a) *Test f* **(b)** *Test g* **(c)** *Test h*

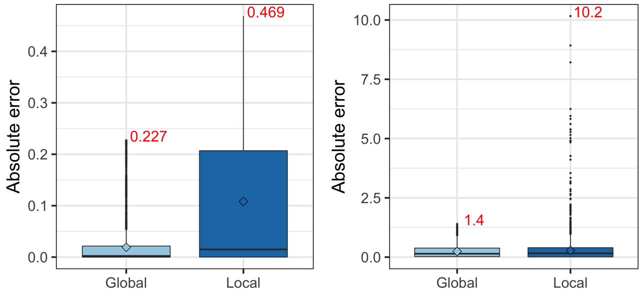

(d) *Test i* **(e)** *Test j*

Figure 24: *Downscaling of the norm of the unit discharge for* `Dam-break` *: box-plots of absolute errors for the global and the local downscaling approaches over the three selected subdomains (375 cells) for each of the five test sets, see Table 4. The maximum error is indicated in red over each box-plot. The scale is capped at 12.*

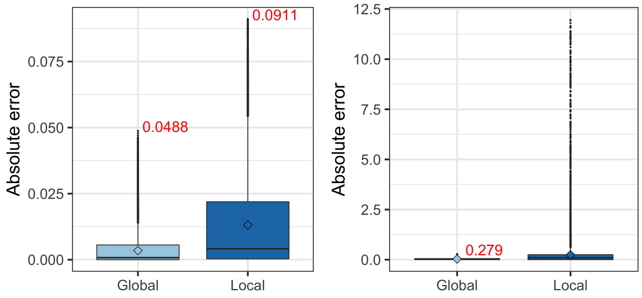

(a) *Test d* **(b)** *Test e*

Figure 25: *Downscaling of the norm of the unit discharge for* `Sacramento` *: box-plots of absolute errors for the global and the local downscaling approaches over the three selected subdomains (375 cells) for each of the five test sets, see Table 4. The maximum error is indicated in red over each box-plot. The scale is capped at 12.*

that summarizes the downscaling model. A key step of this downscaling approach consists in decomposing the high dimensional field into a linear combination of spatial patterns. PCA is often used to obtain spatial patterns from fields of climatic variables in order to infer weather types, i.e. recurring patterns that can be found, for instance, in large scale atmospheric circulation [46]. From the simulated fields of flow variables for urban flood risk assessment, PCA yielded spatial patterns that are visually interpretable with respect to expert knowledge for each configuration and for the two risk variables considered - water depth and norm of the unit discharge, see Figs. 10-17 and Figs. A.26-A.29.

The coefficients of the linear combination of spatial patterns can be thought of as a projection of the high dimensional field onto a low dimensional feature space. In the weather type approach mentioned above, clustering can be performed on the features obtained from PCA to classify each time steps, e.g. days, into weather types. In contrast, in the proposed global downscaling approach, these features are taken as the multivariate dependent variable in a regression model, a feed-forward neural network with a direct linear connection as in Fig. 2b. Model selection, see Table 5, showed that, as was anticipated, more spatial patterns, i.e. a larger dimension of the feature space, are needed to reconstruct the spatial field of more turbulent risk variables. With no hidden units selected in most cases for the ANN, the global approach is in fact a large dimensional multivariate linear regression. The estimation of the model is carried out by combining three steps : (1) PCA of the low resolution field, (2) PCA of the high resolution field and (3) regression between the feature space of the low and high resolution fields. Despite being a linear model, the estimation could not be achieved with a single direct estimation step, as is the case with conventional linear regression, owing to the large dimension of the dependent variable.

We compared the global statistical downscaling approach proposed in this work with a local approach that is in fact a set of downscaling models, one for each cell of the mesh on which the high resolution risk variable is simulated, see subsection 3.1 and Fig. 1a. A potential alternative to this local approach would be to consider a single ANN that would be able to downscale all the cells of the mesh, one at a time, by including in its input specific information from each cell. For instance in [13], a climate variable simulated on a 25 km resolution grid by a Regional Climate Model (RCM) constrained by a GCM on a lower resolution grid of 1.89° is downscaled with a single ANN, one RCM cell at a time. Among the ANN input, there is information from the large scale variable at the four GCM grid cells surrounding the RCM grid cell of interest. By using information that changes with each RCM cell, the ANN is able to learn a relationship that can vary from cell to cell. Such an approach was considered initially in the shallow water models' context but was put aside. Indeed, as the number of cells within each subdomain is very high, the question of which spatial information - geographical coordinates not being sufficient - would be useful to help discriminate each cell has no straightforward answer.

The results from section 5 showed that the proposed global approach yields good overall performance and outperforms in most cases the local approach with an equivalent performance only in a few cases. Nevertheless, absolute errors on test sets can be unacceptably high, e.g.

almost 0.5 m for the water depth in `P-wave-nf`, see Fig. 19b, or about 2 m^2/s for the norm of the unit discharge in `Dam-break`, see Fig. 24b. Further work is needed to understand when and why the global downscaling approach is successful and how to bring improvements when it performs poorly. An interesting avenue of research would be to investigate the representativeness of the spatial pattern basis. Does the training set contain informative enough data to uncover the spatial pattern basis ? In other words, does the training set include all the spatial patterns that are present in the validation and test sets ? Another avenue would be to consider techniques other than PCA to deduce the spatial patterns such as frames [17]. Besides, stochasticity could be introduced in the downscaling methods which would be helpful to account for uncertainties in the estimation. For the local approach, it suffices to see the outputs of the ANN as the parameters of a given probability distribution [10, 12]. For the global approach, the stochastic version of PCA could be implemented [7].

Other perspectives for this work are as follows. The hydraulic simulations reported involve a flat topography. The performance of the downscaling approaches in the case of a variable topography should be explored. In the case of a spatially variable bottom elevation, the free surface elevation is often smoother than the water depth. Whether the surface elevation is easier to downscale than the water depth should be assessed. In addition, imperfect upscaling should be tested as nonlocal effects are to be expected. As mentioned in subsection 2.2, the water depth and the norm of the unit discharge are not the only possible variables for flood risk assessment. The possibility of downscaling additional variables such as the specific force per unit width and the hydraulic head should also be investigated. This might induce an increased level of complexity compared to the downscaling of the water depth and the unit discharge because the specific force and the hydraulic head are not conserved variables. Last, in some cases, only the maximum of a given flow variable within a given area might be needed for risk assessment. In such cases, downscaling techniques developed within the theory of extreme values could be useful [5].

[1] Abt, S.R, Wittler, R.J, Taylor, A, & Love, DJ. 1989. Human Stability in a High Flood Hazard Zone. *Water Resources Bulletin*, **25**, 881–890.

[2] Ayar, P. V., Vrac, M., Bastin, S., Carreau, J., Déqué, M., & Gallardo, C. 2016. Intercomparison of statistical and dynamical downscaling models under the EURO-and MED-CORDEX initiative framework: present climate evaluations. *Climate Dynamics*, **46**(3-4), 1301–1329.

[3] Bates, P.D. 2000. Development and testing of a sub-grid scale model for moving boundary hydrodynamic problems in shallow water. *Hydrol Processes*, **14**, 2073–2088.

[4] Bates, P.D., & De Roo, A.P.J. 2000. A simple raster-based model for flood inundation simulation. *Journal of Hydrology*, **236**, 54–77.

[5] Bechler, A., Vrac, M., & Bel, L. 2015. A spatial hybrid approach for downscaling of extreme precipitation fields. *Journal of Geophysical Research: Atmospheres*, **120**(10), 4534–4550.

[6] Bernardini, G., Postacchii, M., Quagliarini, E., Brocchini, M., Cianca, C., & D'Orazio. 2017. A preliminary combined simulation tool for the risk assessment of pedestrians' flood-induced evacuation. *Environmental Modelling & Software*, **96**, 14–29.

[7] Bishop, C. M. 2011. *Pattern Recognition and Machine Learning.* Information Science and Statistics. Springer.

[8] Blanco-Vogt, A., & Schanze, J. 2014. Assessment of the physical flood susceptibility of buildings on a large scale – conceptual and methodological frameworks. *Nat. Hazards Earth Syst. Sci.*, **14**, 2105–2117.

[9] Bruwier, M., Archambeau, P., Erpicum, S., Pirotton, M., & Dewals, B. 2017. Shallow-water models with anisotropic porosity and merging for flood modelling on Cartesian grids. *Journal of Hydrology*, **554**, 693–709.

[10] Cannon, A. J. 2012. Neural networks for probabilistic environmental prediction: Conditional Density Estimation Network Creation and Evaluation (CaDENCE) in R. *Computers & Geosciences*, **41**, 126–135.

[11] Cannon, A. J. 2018. Multivariate quantile mapping bias correction: an N-dimensional probability density function transform for climate model simulations of multiple variables. *Climate dynamics*, **50**(1-2), 31–49.

[12] Carreau, J., & Vrac, M. 2011. Stochastic downscaling of precipitation with neural network conditional mixture models. *Water Resources Research*, **47**(10).

[13] Chadwick, R., Coppola, E., & Giorgi, F. 2011. An artificial neural network technique for downscaling GCM outputs to RCM spatial scale. *Nonlinear Processes in Geophysics*, **18**(6).

[14] Chanson, H., & Brown, R. 2015. Discussion on "New criterion for the stability of a human body in floodwaters" by Xia et al. (2014). *Journal of Hydraulic Research*, **53**, 540–542.

[15] Chanson, H., Brown, R., & McIntosh, D. 2014. Human body stability in floodwaters: the 2011 flood in Brisbane CBD. *In:* Chanson, H., & Toombes, L. (eds), *Proceedings of the 5th International Symposium on Hydraulic Structures: Engineering Challenges and Extremes.* The University of Queensland, Brisbane.

[16] Chen, A., Evans, B., Djordjevic, S., & Savic, D.A. 2012. A coarse-grid approach to represent building blockage effects in 2D urban flood modelling. *Journal of Hydrology*, **426-427**, 1–16.

[17] Christensen, O. 2008. *Frames and bases: An introductory course.* Springer Science & Business Media.

[18] Cox, R.J., Shand, T.D., & Blacka, M.J. 2010. *Australian Rainfall and Runoff Revision Project 10: Appropriate Safety Criteria for People.* Tech. rept. Report P10/S1/006. AR&R. ISBN 978-085825-9454.

[19] Defina, A. 2000. Two-dimensional shallow flow equations for partially dry areas. *Water Resour Res*, **36**, 3251–3264.

[20] Farmer, C.L. 2002. Upscaling: a review. *International Journal for Numerical Methods in Fluids*, **40**, 63–78.

[21] Foster, D.N., & Cox, R.J. 1973. *Stability of Children on Roads Used as Floodways.* Tech. rept. 73/13. Water Research Laboratory, The University of New South Wales, Manly Vale, NSW, Australia.

[22] Guinot, V. 2012. Multiple porosity shallow water models for macroscopic modelling of urban floods. *Advances in Water Resources*, **37**, 40–72.

[23] Guinot, V. 2017. A critical assessment of flux and source term closures in shallow water models with porosity for urban flood simulations. *Advances in Water Resources*, **109**, 133–157.

[24] Guinot, V., & Soares-Frazão, S. 2006. Flux and source term discretization in two-dimensional shallow water models with porosity on unstructured grids. *International Journal for Numerical Methods in Fluids*, **50**, 309–345.

[25] Guinot, V., B.F., Sanders, & J.E., Schubert. 2017. Dual integral porosity shallow water model for urban flood modelling. *Advances in Water Resources*, **103**, 16–31.

[26] Guinot, V., C., Delenne, & Soares-Frazão, S. 2018. Urban dambreak experiments - RiverFlow paper. *In: RiverFlow 2018 ibternational Conference.*

[27] Hervouët, J.M., Samie, R., & Moreau, B. 2000. Modelling urban areas in dam-break floodwave numerical simulations. *In: Proceedings of the international seminar and workshop on rescue actions based on dambreak flow analysis, Seinâjoki, Finland, 1–6 October 2000.*

[28] Hewitson, B. C., & Crane, R. G. 1996. Climate downscaling: techniques and application. *Climate Research*, **7**(2), 85–95.

[29] Ishigaki, T., Kawanaka, R., Onishi, Y., Shimada, H., Toda, K., & Baba, Y. 2009. *Assessment of Safety on Evacuating Route During Underground Flooding.* Springer, Berlin, Heidelberg. Pages 141–146.

[30] Jongman, B., Kreibich, H., Apel, H., Barredo, J.I., Bates, P.D., Feyen, I., Gericke, A. aned Neal, J., Aerts, J.C.J.H., & Ward, P.J. 2012. Comparative flood damage model assessment: towards a European approach. *Nat. Hazards Earth Syst. Sci.*, **12**, 3733–3752.

[31] Jonkman, S.N., & Penning-Rowsell, E. 2008. Human Instability in Flood Flows. *Journal of the American Water Resources Association*, **44**, 1–11.

[32] Karvonen, R.A., Hepojoki, H.K., Huhta, H.K., & Louhio, A. 2000. *The Use Of Physical Models In Dam-Break Flood Analysis, Development of Rescue Actions Based on Dam-Break Flood Analysis (RESCDAM).* Tech. rept. Helsinki University of Technology, Finnish Environment Institute.

[33] Kim, B., Sanders, B.F., Famiglietti, J.S., & Guinot, V. 2015. Urban flood modeling with porous shallow-water equations: A case study of model errors in the presence of anisotropic porosity. *Journal of Hydrology*, **523**, 680–692.

[34] Matsuo, K., Natainia, L., & Yamada, F. 2011. Flood and evacuation simulations for urban flooding. *Pages 391–398 of:* Chavoschian, A., & Takeuchi, K. (eds), *5th International Conference on Flood Management.*

[35] Merz, B., Kreibich, H., Tieken, A., & Schmidtke, R. 2004. Estimation uncertainty of direct monetary flood damage to buildings. *Natural Hazards and Earth System Sciences*, **4**, 153–163.

[36] Merz, B., Kreibich, H., Schwarze, R., & Thieken, A. 2010. Assessment of economic flood damage. *Nat. Hazards Earth Syst. Sci.*, **10**, 1697–1724.

[37] Rumelhart, D. E., Hinton, G. E., & Williams, R. J. 1988. Learning representations by back-propagating errors. *Cognitive modeling*, **5**, 3.

[38] Sanders, B.F., Schubert, J.E., & Gallegos, H.A. 2008. Integral formulation of shallow water models with anisotropic porosity for urban flood modelling. *Journal of Hydrology*, **362**, 19–38.

[39] Schubert, J.E., Burns, M.J., Fletcher, T.D., & Sanders, B.F. 2017. A framework for the case-specific assessment of Green Infrastructure in mitigating urban flood hazards. *Advances in Water Resources*, **108**, 55–68.

[40] Seifert, I., Kreibich, H., Merz, B., & Thieken, A.H. 2010. Application and validation of FLEMOcs - a flood-loss estimation model for the commercial sector. *Hydrological Sciences Journal*, **55**, 1315–1324.

[41] Takahashi, S., Endoh, K., & Muro, Z-I. 1992. *Experimental Study on People's Safety against Overtopping Waves on Breakwaters.* Tech. rept. Report on the Port and Harbour Institute.

[42] Vrac, M., & Friederichs, P. 2015. Multivariable - intervariable, spatial and temporal - bias correction. *Journal of Climate*, **28**(1), 218–237.

[43] Wagenaar, D., de Jong, J., & Bouwer, L.W. 2017. Multi-variable flood damage modelling with limited data using supervised learning approaches. *Nat. Hazards Earth Syst. Sci.*, **17**, 1683–1696.

[44] Wagenaar, D.J., de Bruijn, K.M., Bouwer, & L.M., de Moel, H. 2016. Uncertainty in flood damage estimates and its potential effect on investment decisions. *Nat. Hazards Earth Syst. Sci.*, **16**, 1–14.

[45] Xia, J., Falconer, R.A., Wang, Y., & Xiao, X. 2014. New Criterion for the Stability of a Human Body in Floodwaters. *Journal of Hydraulic Research*, **52**, 93–104.

[46] Yiou, P., & Nogaj, M. 2004. Extreme climatic events and weather regimes over the North Atlantic : When and where ? *Geophysical Research Letters*, **31**(7).

[47] Özgen, I., Zhao, J., Liang, D., & Hinkelmann, R. 2016. Urban flood modeling using shallow water eqations with depth-dependent anisotropic porosity. *Journal of Hydrology*, **541**, 1165–1184.

Appendix A. Principal spatial patterns

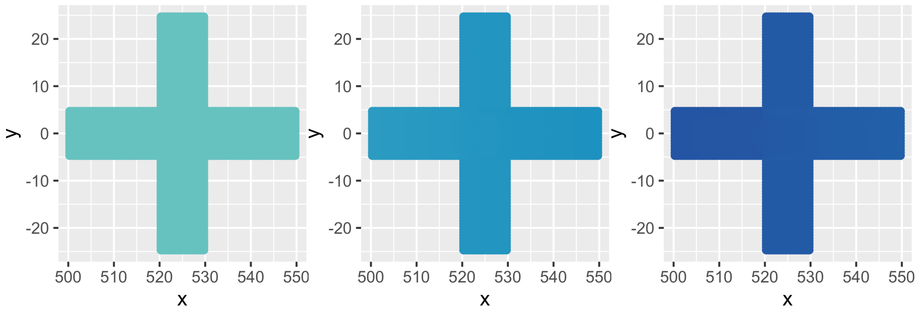

(a) *PC 1* **(b)** *PC 2* **(c)** *PC 3*

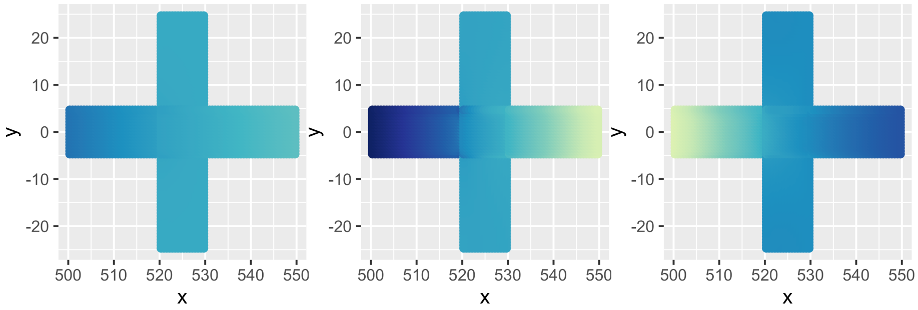

(d) *PC 4* **(e)** *PC 5* **(f)** *PC 6*

Figure A.26: *Spatial patterns of the water depth for* `N-wave-wf` *obtained with PCA (first six PCs) over the subdomain located in the middle of the computational domain. The same adimensional color scale is used for all PCs.*

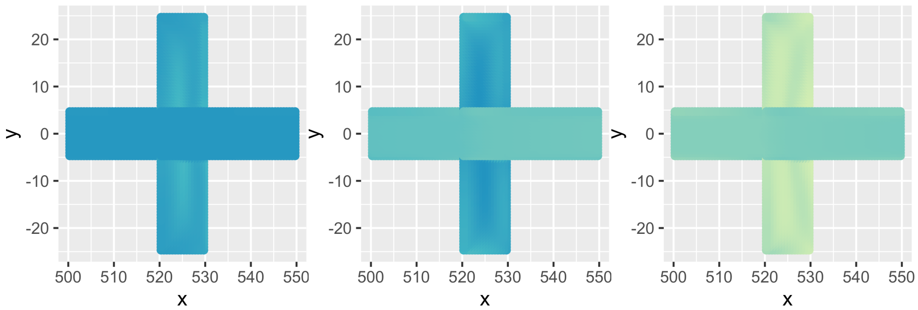

(a) *PC 1* **(b)** *PC 2* **(c)** *PC 3*

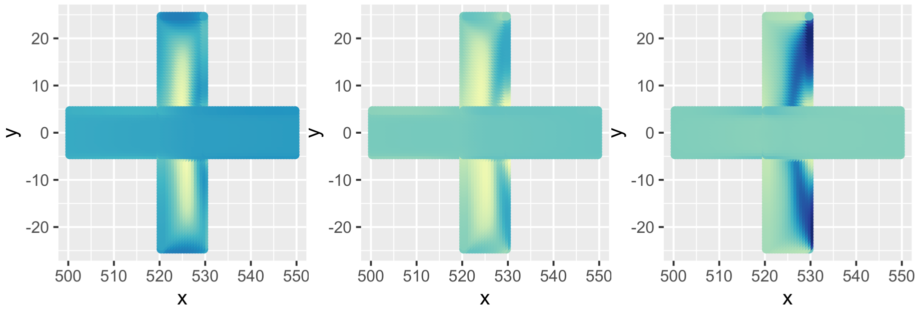

(d) *PC 4* **(e)** *PC 5* **(f)** *PC 6*

Figure A.27: *Spatial patterns of the norm of the unit discharge for* `N-wave-wf` *obtained with PCA (first six PCs) over the subdomain located in the middle of the computational domain. The same adimensional color scale is used for all PCs.*

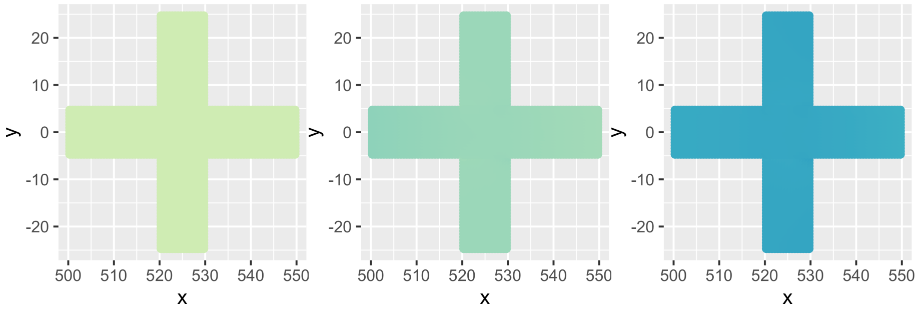

(a) *PC 1* **(b)** *PC 2* **(c)** *PC 3*

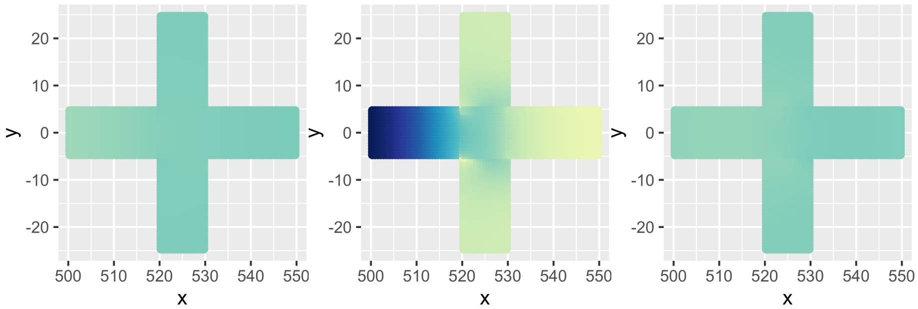

(d) *PC 4* **(e)** *PC 5* **(f)** *PC 6*

Figure A.28: *Spatial patterns of the water depth for* `P-wave-wf` *obtained with PCA (first six PCs) over the subdomain located in the middle of the computational domain. The same adimensional color scale is used for all PCs.*

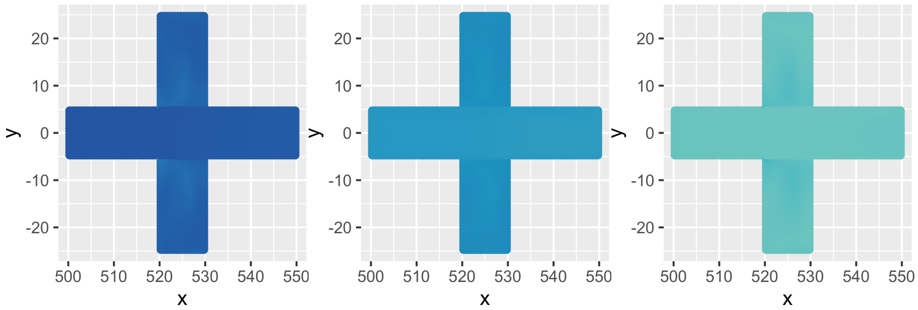

(a) *PC 1* **(b)** *PC 2* **(c)** *PC 3*

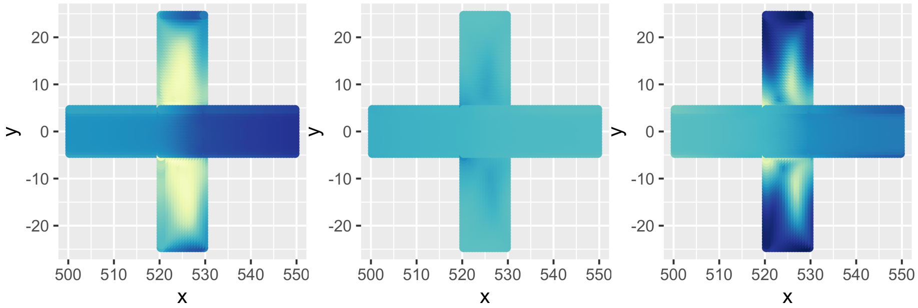

(d) *PC 4* **(e)** *PC 5* **(f)** *PC 6*

Figure A.29: *Spatial patterns of the norm of the unit discharge for* `P-wave-wf` *obtained with PCA (first six PCs) over the subdomain located in the middle of the computational domain. The same adimensional color scale is used for all PCs.*

Appendix B. Evaluation and comparison of downscaling methods

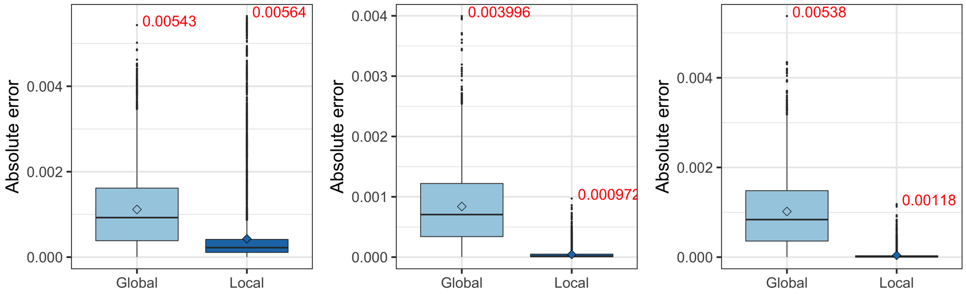

(a) *Test f* **(b)** *Test g* **(c)** *Test h*

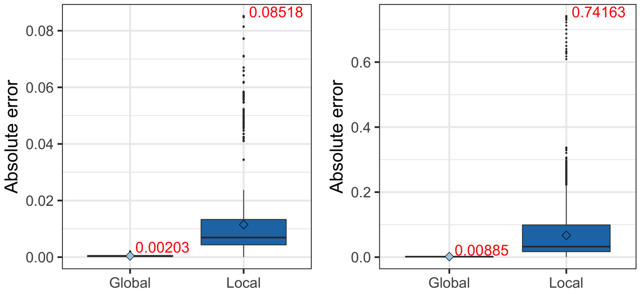

(d) *Test i* **(e)** *Test j*

Figure B.30: *Downscaling of the water depth for* `N-wave-wf` *: box-plots of absolute errors for the global and the local downscaling approaches over the three selected subdomains (375 cells) for each of the five test sets, see Table 4. The maximum error is indicated in red over each box-plot.*

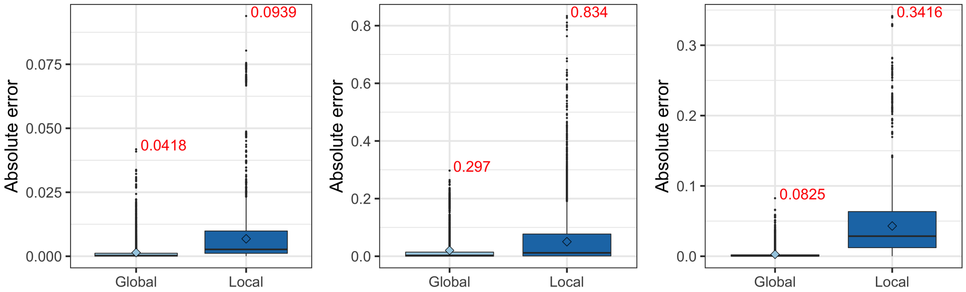

(a) *Test f* **(b)** *Test g* **(c)** *Test h*

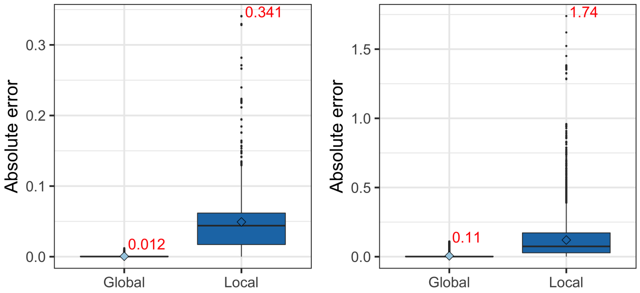

(d) *Test i* **(e)** *Test j*

Figure B.31: *Downscaling of the water depth for* `P-wave-wf` *: box-plots of absolute errors for the global and the local downscaling approaches over the three selected subdomains (375 cells) for each of the five test sets, see Table 4. The maximum error is indicated in red over each box-plot.*

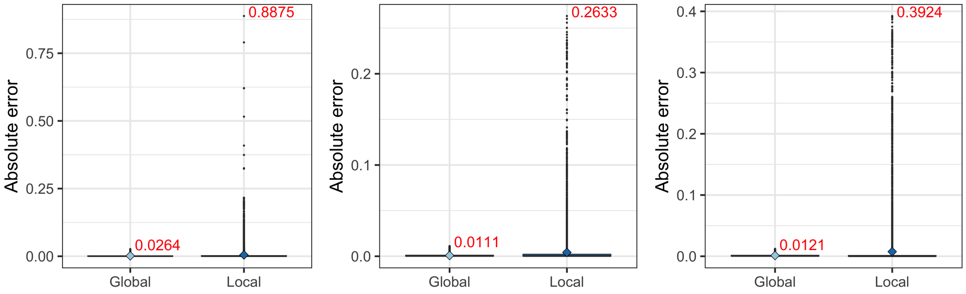

(a) *Test f* **(b)** *Test g* **(c)** *Test h*

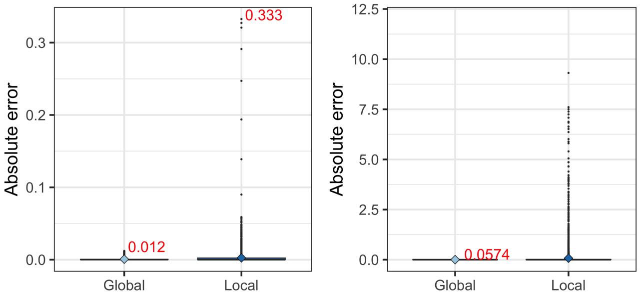

(d) *Test i* **(e)** *Test j*

Figure B.32: *Downscaling of the norm of the unit discharge for* `N-wave-wf` *: box-plots of absolute errors for the global and the local downscaling approaches over the three selected subdomains (375 cells) for each of the five test sets, see Table 4. The maximum error is indicated in red over each box-plot. The scale is capped at 12.*

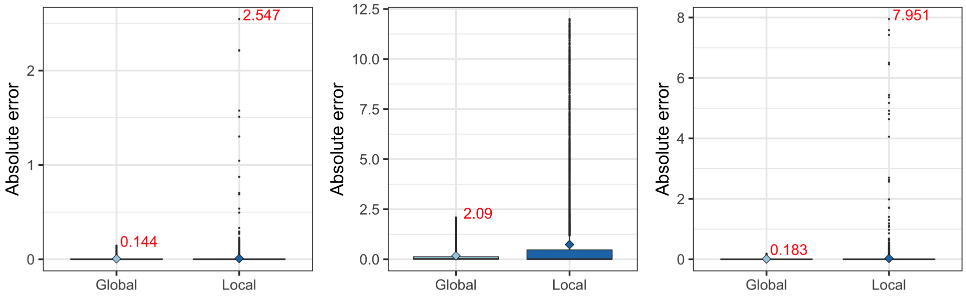

(a) *Test f* **(b)** *Test g* **(c)** *Test h*

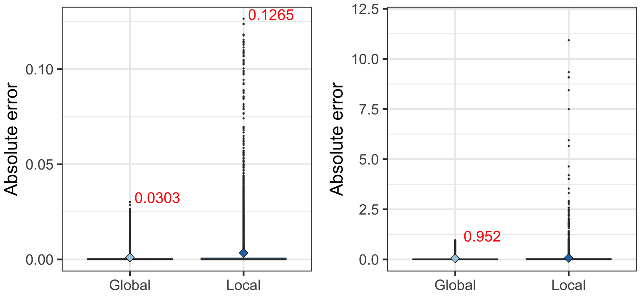

(d) *Test i* **(e)** *Test j*

Figure B.33: *Downscaling of the norm of the unit discharge for* `P-wave-wf` *: box-plots of absolute errors for the global and the local downscaling approaches over the three selected subdomains (375 cells) for each of the five test sets, see Table 4. The maximum error is indicated in red over each box-plot. The scale is capped at 12.*